Geological and Mineralogical Report: Engineer Mine

Leo J. Millonig[1], Lee A. Groat[1] and Robert Linnen[2]

[1]Department of Earth, Ocean and Atmospheric Sciences, University of British Columbia, Vancouver
[2]Department of Earth Science, University of Western Ontario, London

Prepared for BCGold Corp.
Suite 520 – 800 West Pender St.
Vancouver, British Columbia
Canada V6C 2V6

Kirchhain, 2015/03/31

Table of Contents

Appendix A – Microtextures resembling textures observed in V-mica from the Engineer Mine

Appendix B1to B15 – EMP data of sulfides, sulfosalts, alloys and V-mica

Appendix C1 – Geochemistry of Sloko Group volcanics

Appendix C2 – Dike sample localities from the Engineer Mine 5 Level

Appendix D – GEOROC data sets (digital appendix)

Appendix E – Electron-probe micro-analyzer (EMP) operating conditions

Appendix F – LA-ICPMS operating conditions

Summary

The paragenetic sequence for the Engineer and Double Decker Veins indicates that the principal ore assemblage precipitated during a single hydrothermal event. During this event electrum, arsenopyrite, pyrite, ±chalcopyrite, ±sphalerite, ±löllingite, ±tetrahedrite-group phases, ±allargentum, ±acanthite, ±hessite, ±dyscrasite, ±stibarsen, ±galena, as well as unidentified Ag-bearing phases were deposited in conjunction with amorphous silica or chalcedony (now recrystallized to quartz), platy and rhombic calcite, K-feldspar, and (V-)illite. Moreover, textural evidence suggests that besides quartz, calcite and V-illite were also in parts originally precipitated in amorphous form.

The crystallization of platy calcite and K-feldspar, the occurrence of vapor-only fluid inclusions in quartz, the formation of colloform-crustiform vein textures, as well as acicular, skeletal, dendritic, spherical and vermicular crystal habits, indicate that ore-precipitation was caused by supersaturation of the hydrothermal fluid due to rapidly changing P-T-x fluid conditions in response to boiling. Stable isotope analyses, in combination with fluid inclusion studies constrain the ore-forming fluid to a temperature of ~220 °C and an isotopic composition (δ^{18}O and δD) similar to meteoric water. Furthermore, carbon and oxygen isotope analyses of vein and sedimentary carbonate minerals indicate that the hydrothermal fluid attained its δ^{18}O and δ^{13}C composition due to prolonged interaction with the host rocks.

Based on vein textures, mineralogy and fluid inclusion studies the Engineer Mine is classified as an epithermal low-sulfidation deposit. Furthermore, the fact that the Engineer Mine shares similarities with alkaline, as well as subalkaline epithermal low-sulfidation deposits, *e.g.,* in terms of ore and gangue phases and fluid inclusions, is due to the fact that the Sloko-Skukum Group volcanics are borderline subalkaline to alkaline in character.

Objective

Gold-bearing quartz-carbonate veins at the Engineer Mine feature roscoelite (V-mica), an association which occurs at only a few other localities worldwide. The occurrence of roscoelite in conjunction with telluride-rich mineralization and fluorite is characteristic for precious metal deposits related to alkaline magmatism (Jensen and Barton, 2000). Prominent examples for this deposit type include Cripple Creek, Colorado, the Emperor deposit, Fiji (Jensen, 2008), and Porgera, Papua New Guinea (Jensen and Barton, 2000) (Table 1). However, although the mineralization at the Engineer Mine shares features characteristic for the alkaline-epithermal deposit type, such as the occurrence of roscoelite, it lacks others, such as the presence of tellurides (Mauthner et al., 1996). The purpose of this study is to clarify these ambiguities and to properly classify the Engineer Mine deposit considering its structural setting, mineralogy and conditions of formation. This study focusses in particular on answering the following questions:

(1) What is the mineralogy and geochemistry of the veins? What does this tell us about the source of the gold?
(2) At what temperature and pressure did the veins form?

4

(3) What are the structural and spatial relationships between the geologic features of the area (i.e., veins, dykes, deformational events, etc.)?

(4) What is the chronology of the formation and/or emplacement of the geologic features?

As there are some data available for questions (3) and (4), this project placed the highest priority on questions (1) and (2).

A thorough understanding of these variables is envisaged to aid the exploration and exploitation of the deposit. This study was jointly and generously funded by BCGold Corp. and Mitacs, a national, not-for-profit organization.

Table 1. Historic gold production of gold deposits related to alkaline magmatism.

Deposit name	Operator	Historic gold production	Reference
Cripple Creek, CO, USA	Cripple Creek and Victor Gold Mining Company	>4.5 Moz (1995-2013) ~21 Moz in the mining district	http://ccvgoldmining.com/ccvmodernmining.html and https://coloradomining.org/content/programs_pdf/ccv-ops_billingsley.pdf
Emperor, Vatukoula, Fiji	Vatukoula Gold Mines Plc	>7 Moz (until 2014)	http://www.vgmplc.com/
Porgera, Papua New Guinea	Barrick Gold (95%), Mineral Resource Enga (MRE) (5%)	>17.4 Moz (until 2011)	Rennie et al. (2012)

Methods

Drill core samples with elevated Au, Ag, Sb, and/or As-contents from the Engineer and Double Decker Veins were investigated in this study. In addition, vein material from the 5th, 6th and 7th mine level, the 505-3A and 3B stope bulk samples (Fig. 1), surface outcrops of the Engineer and Double Decker Veins, as well as heavy mineral separates from the 5th mine level bulk samples (Fig. 1) were studied. The latter represent a cross section of the various vein stages and also contain phases belonging to the (altered) country rock. Thus, they complement the other samples, but an assignment of individual minerals to certain vein stages is not always unambiguously possible. The collected samples range over ~150 m vertically and 400 m along strike. Structural (Devine, 2008) and mineralogical (this study) similarities between the Engineer and Double Decker Veins suggest that they formed during the same hydrothermal event.

In order to establish the paragenetic sequence, hand specimens were investigated at the University of British Columbia (UBC) using the naked eye and a stereoscopic microscope. To further characterize the ore and gangue phases and to identify samples suitable for fluid inclusion studies, polished thin sections of selected areas were prepared. These thin sections were then investigated at UBC using optical (Nikon Eclipse E600) and scanning electron microscopes (SEM; Philips XL-30).

The chemical compositions of sulfides, sulfosalts, alloys and V-mica were determined at the UBC using a fully automated CAMECA SX-50 electron-probe micro-analyzer (EMP) (Appendix E).

Fluid inclusion studies were conducted at the University of Western Ontario (UWO) with a Linkham THMSG600 heating-freezing stage.

Different carbonate generations were distinguished in drill core and hand specimen using normal and UV-light, and analyzed for C- and O-isotopic compositions at UBC using off-axis integrated cavity output spectroscopy (OA-ICOS; Los Gatos Research, model 908-0021) following the method of Barker et al. (2011). Isotopic ratios are reported in per mil (‰) relative to the international standard of Vienna-standard mean ocean water (V-SMOW) for oxygen and PeeDee belemnite (PDB) for carbon using the conventional delta notation. The internal precision (1σ) is <0.5‰ for $\delta^{13}C_{VPDP}$ and <0.6‰ for $\delta^{18}O_{VSMOW}$ (Barker et al., 2011).

Vanadium mica, associated with visible electrum, was separated, hand-picked under the microscope, and analyzed for its hydrogen and oxygen isotope composition at Queen's Facility for Isotope Research (QFIR), Queen's University, Kingston. Isotopic ratios are reported in per mil (‰) relative to the international standard of V-SMOW for oxygen and hydrogen using the conventional delta notation. The analytical precision is ±0.1‰ and ±1‰ for $\delta^{18}O$ and δD, respectively.

In-situ trace element analyses of thin sections and grain mounts of sulfides, sulfosalts and alloys were conducted at the Geological Survey of Canada, Ottawa using Laser Ablation Inductively Coupled Plasma Mass Spectrometry (LA-ICPMS) (Appendix F).

History of the Engineer Mine and Resource Estimates

Precious metal-bearing vein material at what was to become the Engineer Mine (Fig. 1) was first discovered by surveyors for the White Pass and Yukon Railway in 1899 (Mauthner et al., 1996). Intermittent mine development and production, mainly from the Engineer and Double Decker Veins, followed and peaked between 1913-1918 and 1925-1927 (Mihlaynuk et al., 1999; Dominy and Platten, 2011). Production between 1913 and 1952 yielded 560 kilograms (kg) gold and 280 kg silver, with average grades of 36 g/t Au and 18 g/t Ag (Mihalynuk et al., 1999a). Currently the Engineer Mine property is 100% owned by BCGold Corp., headquartered in Vancouver, B.C. Recent exploration programs conducted by BCGold Corp. include: diamond drilling programs in 2008 and 2010, targeting Shear-A and the Engineer and Double Decker Veins, respectively; Surface and underground mapping in 2010; a bulk sampling program in 2011 (Fig. 1), as well as a sampling and dewatering program of the 6 and 7 level in 2012. A NI43-101 compliant resource estimate, commissioned by BCGold Corp. and calculated by Dominy and Platten (2011), provides for a combined inferred resource of 41,000 tonnes grading 19 g/t Au (cut-off of 5 g/t Au), including 14,000 tonnes grading 52.5 g/t Au (cut-off of 25 g/t Au) for the Engineer and Double Decker Veins (Fig. 1). Silver/gold ratios of quartz-carbonate lode veins at the Engineer Mine, based on historic production figures, range between 0.5 and 0.9 (Mihalynuk et al., 1999a).
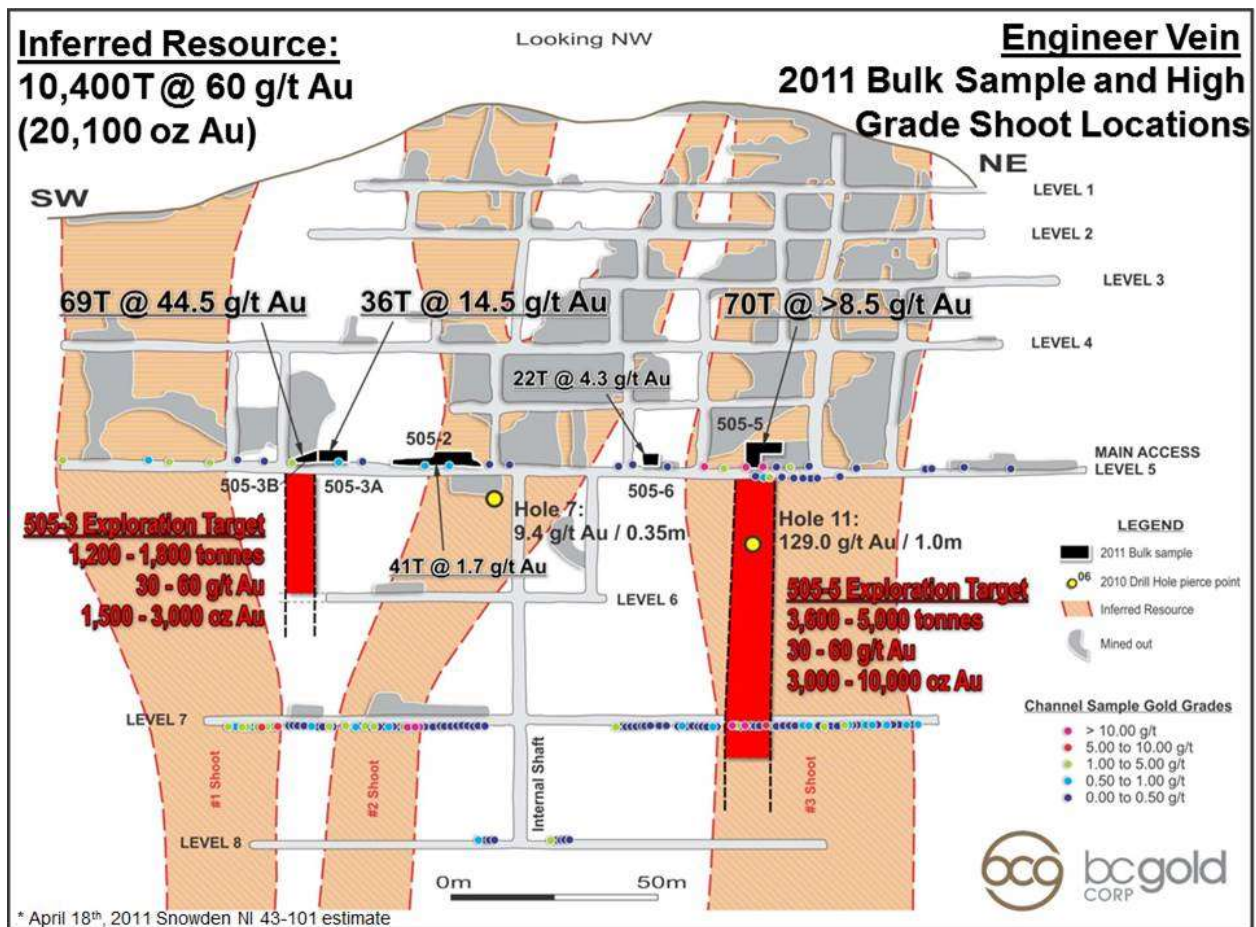
Fig. 1: Long section of the Engineer Vein workings, 2011 bulk sample locations (black boxes), inferred resource and exploration targets (BCGold Corp., 2015; Dominy and Platten, 2011).

Regional, Local and Mine Geology

Detailed studies of the regional and local geology of the Engineer Mine area are presented in Mihalynuk et al. (1999a) and Devine (2008), respectively.

The Engineer Gold Mine is located in northern British Columbia, Canada, on the southeastern shore of Tagish Lake (Fig. 2), about 135 km south of Whitehorse and 32 km west of Atlin. It is situated within the Whitehorse Trough, which comprises Stuhini Group and Laberge Group strata (Fig. 2). The Triassic Stuhini Group lithologies are diverse and include basic to intermediate subalkaline volcanic flows, pyroclastics and related arc sediments (Mihalynuk et al., 1999a). In contrast, Jurrasic Laberge Group strata are dominated by immature marine clastics, such as conglomerates, greywackes and argillites (Mihalynuk et al., 1999a). The Whitehorse Trough is bounded by two major, north-northwest-trending faults, the Llewellyn and the Nahlin Fault, which separated it from the Yukon-Tanana Terrane to the west and the Cache Creek Terrane to the East, respectively (Mihalynuk et al., 1999a). The precious metal-bearing quartz-carbonate ± roscoelite veins are hosted in Lower Jurassic Laberge Group argillite and greywacke (Devine, 2008). These veins are inferred to have formed during Eocene reactivation of the crustal-scale Llewellyn fault and

7

associated splays, and coeval hydrothermal activity related to Sloko Groups magmatism in a continental arc setting at ~55 Ma (Mihalynuk et al., 1999a; Devine, 2008). A precious metal deposit, also related to Sloko Group magmatism and sharing many similarities with the Engineer Mine is the epithermal Mt. Skukum gold deposit in the Yukon, located c. 100 km to the NNW (Mihalynuk et al., 1999a).
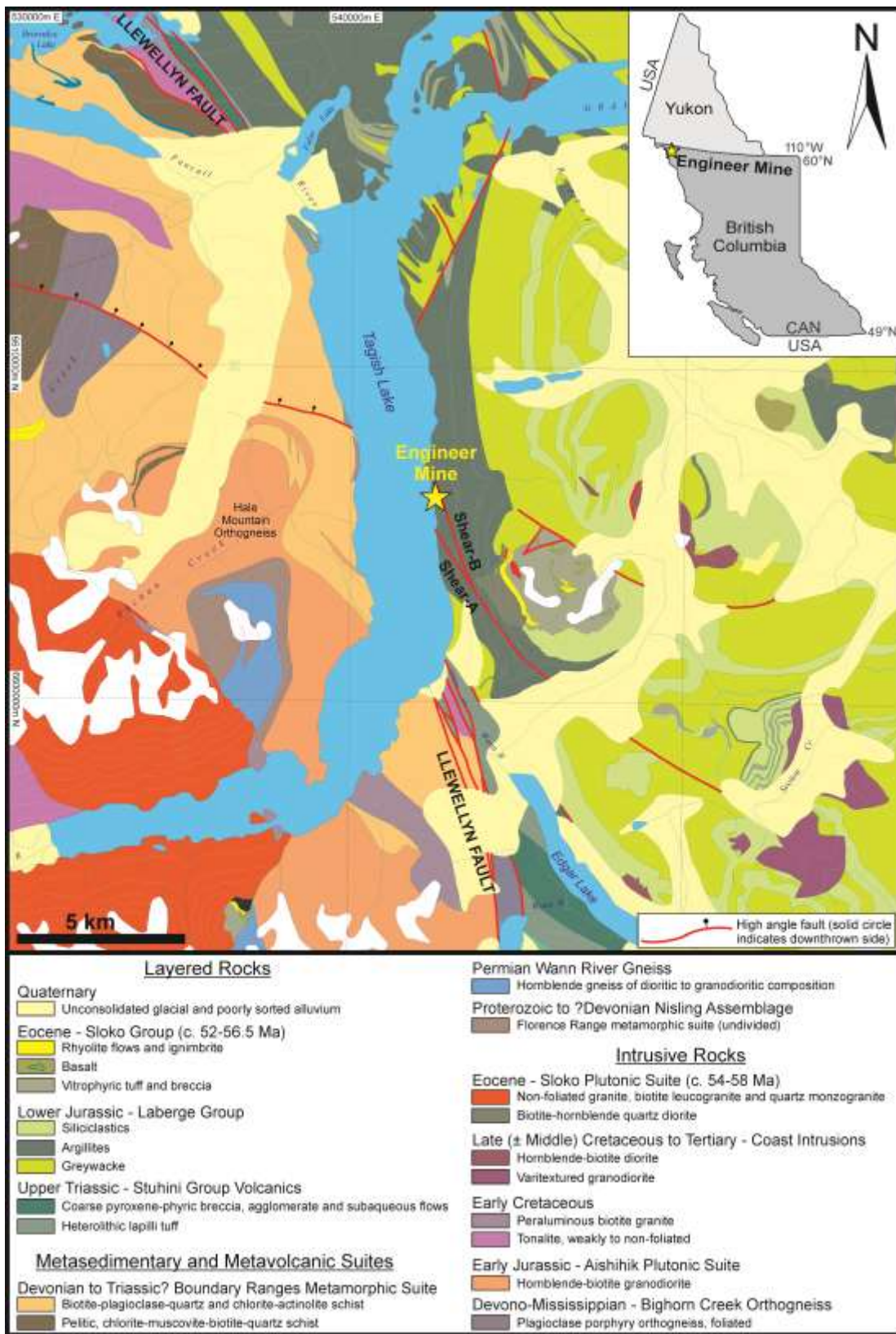
Fig. 2: Index map and simplified geological map of the Tagish Lake area showing major lithologies, faults, and the location of the Engineer Mine (modified after Mihalynuk et al., 1999a).

Based on fluid inclusion data, the estimated depth of vein formation and its mineralogy, the Engineer Mine is suggested to be a transitional meso- to epithermal low sulfidation deposit, formed at ≤197 °C and ~1.8 km depth (Mihalynuk et al., 1999a). Vein textures, such as open space fillings are more characteristic of a shallower setting (Devine, 2008; Jensen, 2008), however, and the synchronous development of the hydrothermal system with structural reactivation of the regional Llewellyn fault and associated structures such as Shear-A (Figs. 2 and 3; Mihalynuk et al., 1999a) may account for textural and depth ambiguities (Devine, 2008).

Volcanic and intrusive rocks

Erosional remnants of the flat-lying, formerly extensive Sloko Group volcanics exist on top of Engineer Mountain, situated 1-2 km southeast of the Engineer Mine (Fig. 2). The volcanic rocks are comprised of rhyolite to andesite flows, breccia, tuffs, ignimbrite and coeval intrusions. U-Pb dating of zircon from the rhyolite unit yielded an age of 54.1 ± 0.1 Ma (Gabites, 1999; in Mihalynuk et al., 1999b).

Three successive generations of monzodiorite dykes cut the Laberge Group sedimentary rocks at the Engineer Mine property and are inferred to be genetically related to the Sloko Group volcanism (Devine, 2008). Field relations indicate that the oldest dykes pre-date the main hydrothermal event and caused carbonate-quartz-pyrrhotite, and possibly chalcopyrite (Jensen, 2008) alteration of Laberge Group rocks (Devine, 2008). In contrast, the youngest dykes overlap with the earliest stages of hydrothermal activity in the area (Devine, 2008). An K/Ar-Ar roscoelite age of 49.9 Ma (Devine, unpublished data), interpreted to date the ore-forming event, postdates Sloko Group volcanism by ~4 Ma. The frequent spatial association between the monzodiorite dykes and Au-Ag-bearing quartz-carbonate veins suggests that vein formation was in places facilitated by, and locally followed, pre-existing zones of structural weakness between dyke and host rock. Age and field relations therefore suggest that the precious metal-bearing veins developed during the waning stages of Sloko Group volcanism.

Structural features

Eocene fault reactivation, concomitant with Sloko Group volcanism, promoted the emplacement of the epithermal veins and is considered a controlling factor for the emplacement and orientation of the Engineer and Double Decker Veins (Devine, 2008). The main structural feature on the Engineer Mine property is referred to as Shear Zone A (Shear-A; Fig. 3). According to Devine (2008), Shear-A is a northwest-trending splay of the Llewellyn Fault (see also Schroeter, 1986) that records two distinct periods of deformation: (1) Middle Jurassic to possibly Cretaceous right-lateral semi-brittle displacement in a 150 m wide zone, and (2) Early Eocene reactivation along its north-eastern margin with brittle right-lateral displacement focused in a relatively narrow zone.
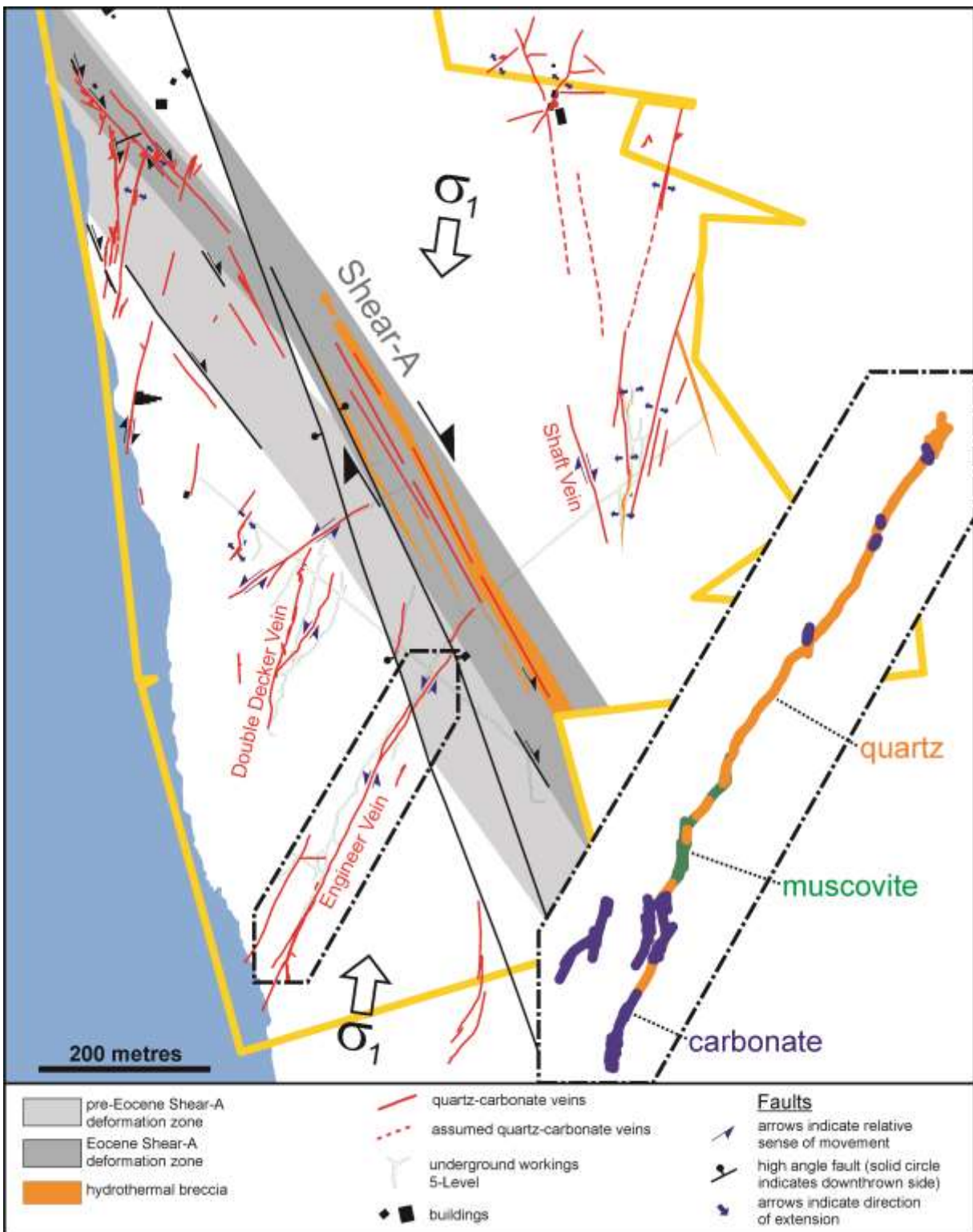
Fig. 3: Overview of veins and structural features at the Engineer Mine. Inset (dash-dot line) shows distribution of main gangue phases of the Engineer Vein on the 5th Mine level. Modified after Devine (2008). The thick yellow line indicates Engineer Mine property boundaries as in 2012.

Host rocks

Host rocks to the precious metal veins at the Engineer Mine are the Laberge Group sedimentary rocks (Fig. 2), which consist of grey to brown well-bedded argillite and fine-grained greywacke with locally developed calcareous beds and a wide pale beige to buff-coloured feldspathic arenite layer. In addition, a massive and locally laminated fine-grained dark carbonaceous argillite unit with abundant disseminated pyrite can be distinguished (Devine, 2008). This carbonaceous unit possibly promoted V-mica and gold precipitation due to its reducing capacity, as suggested by the location of the 'bonanza zone' of the Engineer Vein at the lithological contact between this unit and the well-bedded argillite to fine-grained greywacke unit (Devine, 2008).

Epithermal Veins

Numerous quartz-dominated veins occur at the Engineer Mine property (Fig. 3) and are discussed in detail by Devine (2008). The description below focusses on the Engineer and Double Decker Vein (see Devine, 2008).

The Engineer Vein (E-Vein) is the historically most productive and largest vein with a strike length of 400 m and ca. 5 cm to 2 m width. It has been mined vertically for over 100 m and remains open to depth (Fig. 1). Vein textures are dominantly extensional and the vein offsets intrusive units, indicating sinistral movement during vein formation, similar to the Double Decker Vein (Fig. 4a). The E-Vein is regarded as the longest-lived vein in the system (Devine, 2008) and shows a complex evolution of various stages of mineral precipitation and replacement. Notably, quartz-cemented hydrothermal breccias with rounded to subangular clasts of a variety of earlier vein stages are unique to the E-Vein (Fig. 4b; cf. Figure 23E of Devine, 2008), and electrum is typically in direct contact with roscoelite. Bladed calcite (Fig. 4c) and quartz pseudomorphs after bladed calcite have been reported from the E-Vein by Jensen (2008). The widest and most productive ore-shoots within the E-Vein occur where the vein is kinked to form extensional jogs, or in close proximity to vein-parallel dykes.

The Double Decker Vein (DD-Vein) is a set of at least three anastamosing en-echelon quartz-carbonate veins 10 cm to 1.5 m wide that dip 80 to 50 degrees southeast. Vein textures are dominantly extensional (Fig. 4a), with local evidence for sinistral reverse movement across the veins. Historically, the best gold grades were obtained where the vein was widest (Devine, 2008). The vein pinches and swells along strike and several different phases of quartz and carbonate precipitation can be distinguished. Hydrothermal brecciation of the wall rock during initial vein opening is generally followed by open-space in-filling comb-textured quartz. Subsequently several phases of drusy quartz and fine carbonate were deposited in open spaces. In addition, bands of green white mica and quartz are locally developed. Gold/electrum in the DD-Vein commonly occurs as free gold in quartz, but also in association with roscoelite and allemontite.
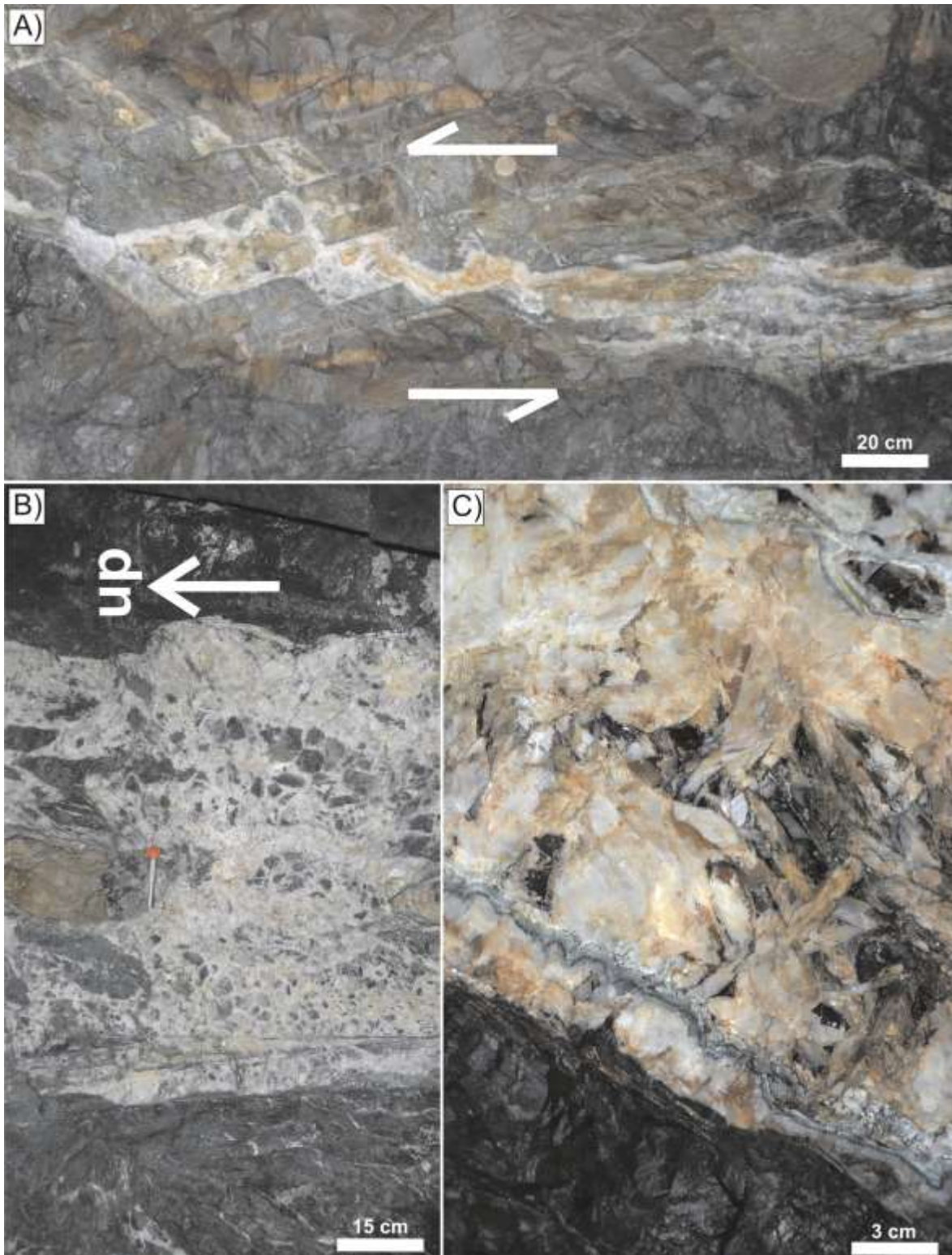
Fig. 4: Vein textures of the Double Decker (A) and Engineer (B and C) veins highlighting their textural and mineralogical variability. (A) Back of a drift (5th mine level) showing dilatational jogs due to sinistral strike-slip faulting. This faulting created the space for hydrothermal fluids to precipitate ore and gangue phases (see Discussion). (B) Vertical vein intersection with abundant brecciated host rock fragments cemented by quartz ± carbonate (7th mine level). The central vug just left of the scale (pen) is ~15 cm wide. (C) Calcite-dominated interval of the E-Vein (5th mine level). Note the development of platy (bladed) calcite in the center-right of the image and its intergrowth with

13

rhombic calcite toward the edge of the vein. In the lower-right corner the ore-forming stage, represented by quartz and V-mica (grey-green colloform-crustiform texture), precipitated directly onto the host argillite, whereas to the left rhombic calcite precipitated first. This illustrates the fact that not all vein stages are present at any one locality.

Mineralogy of the Epithermal Veins

Prior to this study Mauthner et al. (1996) presented the most comprehensive study of the mineralogy of the epithermal veins at the Engineer Mine. They identified electrum, native antimony, native arsenic interlayered with stibarsen (formerly referred to as 'allemontite'; cf. Mauthner et al, 1996), arsenopyrite, löllingite, pyrite, pyrrhotite, quartz, calcite, ankerite, siderite, fluorite and roscoelite. In contrast, the presence of native bismuth, stibnite, tellurides and mariposite, as reported in earlier studies (see Mauthner et al., 1996), could not be confirmed and were most likely originally misidentified according to Mauthner et al. (1996). Chalcopyrite was reported in the B.C. Mines Annual Report (1927), observed in a surface trench in the DD-Vein and noted in core logs of BCGold Corp.'s 2008 drilling program, which targeted Shear-A. In the latter, the paragenesis chalcopyrite-pyrite-pyrrhotite, in association with 'calc-silicate patches', suggests that these sulfide minerals are related to the carbonate-quartz-pyrrhotite alteration, as described above and in Devine (2008) (cf. Jensen, 2008). This alteration, however, occurs in the wall rock only and predates the formation of the epithermal veins. Furthermore, berthierite was identified by Schroeter (1986), and Smit (1988) noted tetrahedrite in vein intersections of drill hole 87-102 north of Shear-A. These intersections are most likely related to the Shaft Vein (Fig. 3). Muscovite/sericite and aragonite were identified in vein samples investigated by Payne (2007; in Aspinall, 2007), and Leitch (2012) reported marcasite, K-feldspar and rutile. Realgar was observed on fractures in drill hole DDH BCGE08-07 (Devine, 2008). In some instances staining of vein material indicates the presence of substantial amounts of K-feldspar (sample 11FD206of Leitch, 2012), whereas in other samples no K-feldspar could be detected (samples E-88482 and E-88492 of Aspinall, 2007).

Unfortunately, and with the exception of Smit (1988) and BCGold Corp.'s 2008 drill core logs (Devine 2008), the aforementioned studies do not state from which part of the Engineer Mine the investigated samples originated and the identified phases may therefore belong to different stages of vein formation and/or different veins. Hence, a systematic investigation of the vein mineralogy is needed.

Paragenetic sequence

The paragenetic sequence of the Engineer Mine epithermal system was established based on macro- and microscopic observations of 27 samples from the E-Vein. A general characteristic is that the width of the vein broadly correlates with the number of distinguishable stages, i.e., the wider the vein, the more complex its evolution. This is attributed to the channeling of fluids along major pathways that are repetitively activated during the lifetime of the epithermal system. Furthermore, mineral replacement (Mauthner et al., 1996), alteration and brecciation (Fig. 4) due to successive hydrothermal events commonly obscure earlier textures. The point made by Ahmad et al. (1987) with respect to the epithermal Emperor deposit, Fiji, that '*not all vein stages can be recognized at any one place*' and that '*it is possible that at any time different assemblages were forming in*

different parts of the mine' is also applicable to the epithermal veins at the Engineer Mine. The lateral variability of the E-Vein, with respect to the dominant gangue phases, quartz, carbonate and muscovite, is shown in Figure 3. Vein and mineral textures of the various vein stages, as discussed in the following, are shown in Figure 6.

Pre-vein formation

Prior to formation of the epithermal veins, the argillite host rocks were locally altered by 'calc-silicate' carbonate-pyrrhotite ± quartz ± pyrite ± chalcopyrite alteration, causing bleaching of the host rock due to the formation of clay alteration halos (Fig. 5) (Devine, 2008; Jensen, 2008). This alteration is attributed to the emplacement of dikes of the Sloko Group (Coates, 2015; personal communication). During subsequent vein formation these altered rocks were in parts been fragmented and incorporated in the epithermal veins.
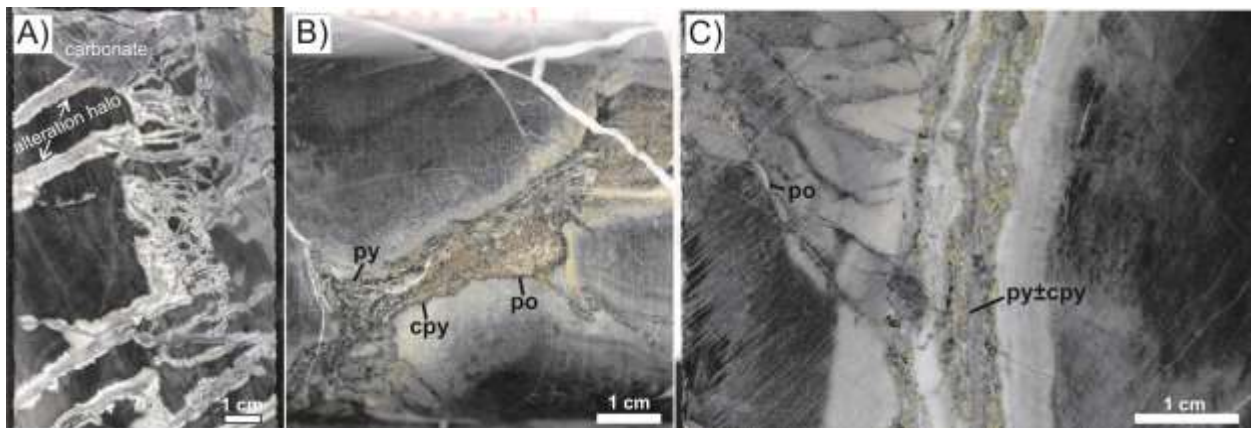

Fig. 5: Drill core samples showing the early alteration of the host argillite, prior to the formation of the epithermal veins, characterized by carbonate-pyrrhotite ± pyrite ± chalcopyrite and the development of clay alteration halos. (A) Intense but narrow clay halos around carbonate (dark bluish-grey). (B) A veinlet of carbonate-pyrrhotite ± pyrite ± chalcopyrite and its surrounding clay halo is cut by a later carbonate veinlet (white). (C) A network of carbonate-sulfide veinlets causes pronounced, but localized, bleaching of the host argillite due to clay alteration.

Vein formation

The paragenetic sequence for the precious metal-bearing epithermal veins, starting at the vein wall, is:

(I)   Brecciation, silicification, and cementation of wall rock clasts by very fine-grained grey transparent quartz, locally accompanied by arsenopyrite and pyrite. The wall rock clasts are commonly bleached and sulfide-bearing due to the earlier carbonate-pyrrhotite alteration (see above). Quartz of this stage is interpreted to be recrystallized amorphous silica or chalcedony. In other places coarse-grained eu- to subhedral rhombic carbonate is developed at this stage (Fig. 4c).

(II)   Brecciation (locally developed) and deposition of amorphous silica or chalcedony (now recrystallized to grey transparent quartz) together with dark-green V-bearing mica, ±electrum, ±K-feldspar (adularia), pyrite, arsenopyrite, ±löllingite/geyerite, ±chalcopyrite, ±tetrahedrite, ±acanthite, ±allargentum, ±sphalerite, ±hessite, ±dyscrasite,

±galena and minor calcite. This stage produced characteristic colloform, crustiform and cockade textures (Figs. 4c and 6a, c, d). The V-mica occurs in thin bands (Figs. 6c and d), or is massive and commonly is closely associated with electrum and (altered) K-feldspar (Fig. 6e). The order of deposition in this main ore-forming stage is V-mica ±electrum ±amorphous silica followed by K-feldspar ±calcite and amorphous silica ±arsenopyrite ±V-poor mica (Figs. 6c to e). The latter paragenesis of amorphous silica ±arsenopyrite ±V-poor mica commonly precipitated repetitively, causing crustiform textures (Figs. 6a and d).

(III) Fine- to coarse-grained rhombic and platy calcite, which has mostly been replaced by quartz (Fig. 6a).

(IV) Light-green to grey-white amorphous silica or chalcedony (Fig. 6d), which mostly recrystallized to quartz. The color of individual bands is caused by the presence of disseminated V-poor mica, and/or minor amounts of sulfide and sulfosalt minerals and alloys, such as pyrite, chalcopyrite, arsenopyrite, tetrahedrite-group phases, allargentum and rare electrum, in quartz. Amorphous silica/quartz of this stage formed thin colloform layers (Fig. 6d), or extensively replaced bladed and rhombic calcite of stage (III) (Fig. 6a). Rare stibarsen ('allemontite') is also interpreted to belong to this stage (cf. Devine, 2008).

(V) Local brecciation and deposition of coarse-grained white massive carbonate with rhombic and, in open space, platy habit (Figs. 4c and 6a). It is important to note that textural relationships suggest that stages (II) to (V) formed in close succession and are interpreted to be part of the same hydrothermal event.

(VI) White-grey to orange-brown transparent amorphous silica or chalcedony, and minor arsenopyrite, pyrite, ±chalcopyrite. The amorphous silica or chalcedony recrystallized to quartz and replaced earlier calcite (Fig. 6a).

(VII) Orange-brown Fe-carbonates as central bands in veins (Fig. 3a; cf. Jensen, 2008), or infill in vugs (Fig. 6c).

(VIII) Open space fillings of white to transparent calcite, cream-colored ankerite or dark red-brown siderite, quartz, and/or pyrite. Individual calcite crystals can attain several cm in size and may be coated by quartz, which in turn may be coated by siderite and pyrite (Fig. 7). Usually several generations of these late, mostly euhedral phases occur together in the same vug. This stage occurred late, during or after the main epithermal vein formation.
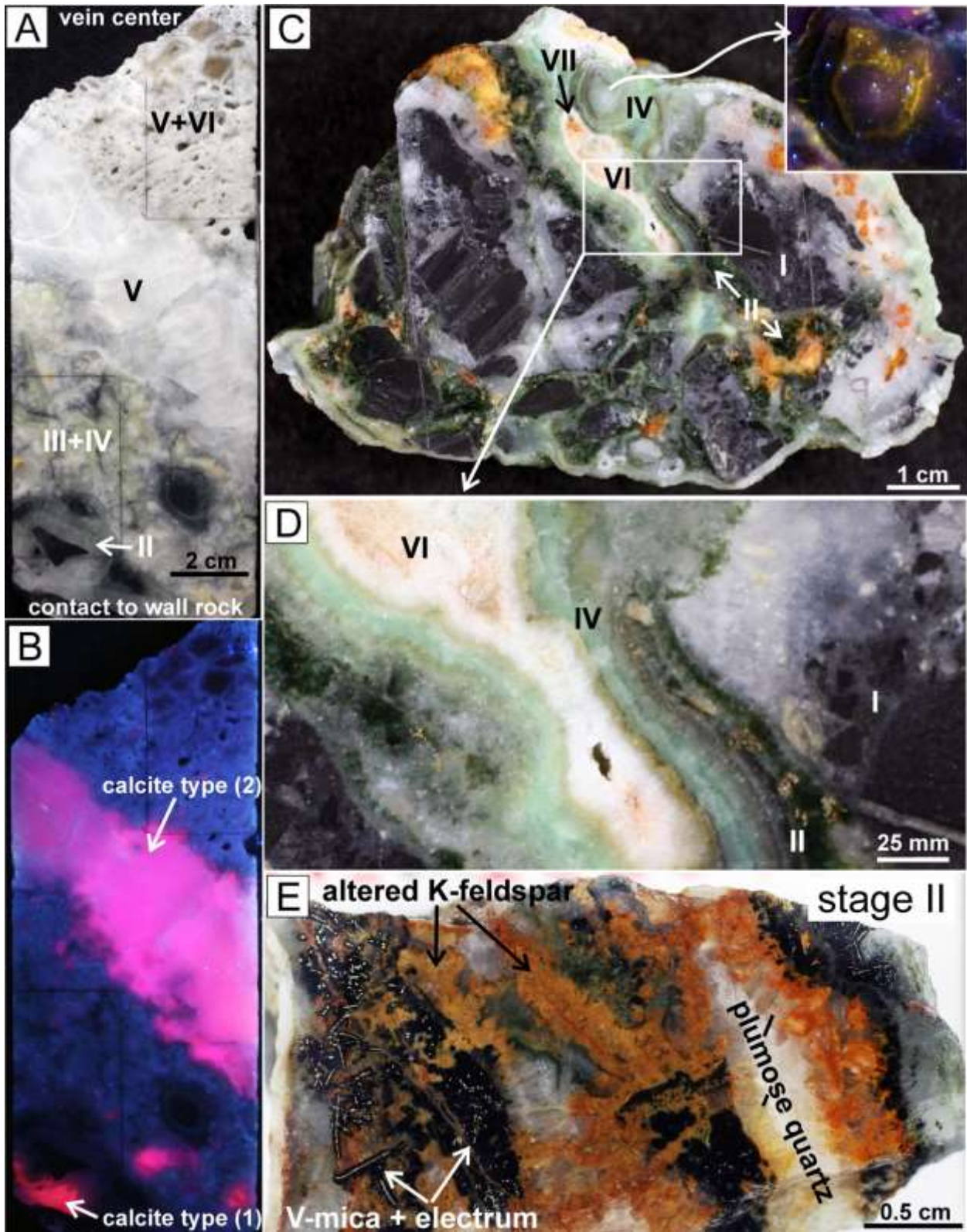
Fig. 6: Vein samples from the Engineer Vein showing various stages of vein development. (A) Cockade textures formed during stage (II) and replacement of stage (III) and (V) calcite by stage (IV) and (VI) quartz, respectively. Note the development of rhombic and platy calcite during stage (V). The latter formed toward the vein center and was preferentially replaced by (lattice) quartz. (B) same as (A), but under UV light, showing two optically different generations of vein calcite. (C) Complex sample showing early brecciation during stage (I) and (II), as well as dark

green V-mica and (altered) K-feldspar (orange-brown) deposited during the main ore-forming stage (II). Carbonate of the early vein stages is not developed in this sample. The inset shows the fluorescence of stage (IV) chalcedony under UV light. (D) Detail of (C) showing colloform banding developed during stages (II) and (IV), as well as stage (II) V-mica associated with ore phases (pyrite, arsenopyrite, chalcopyrite, tetrahedrite-group minerals). (E) Typical mineral assemblage precipitated during the main ore forming stage (II) with electrum in dark-green V-mica, surrounded by (altered) K-feldspar and recrystallized quartz.
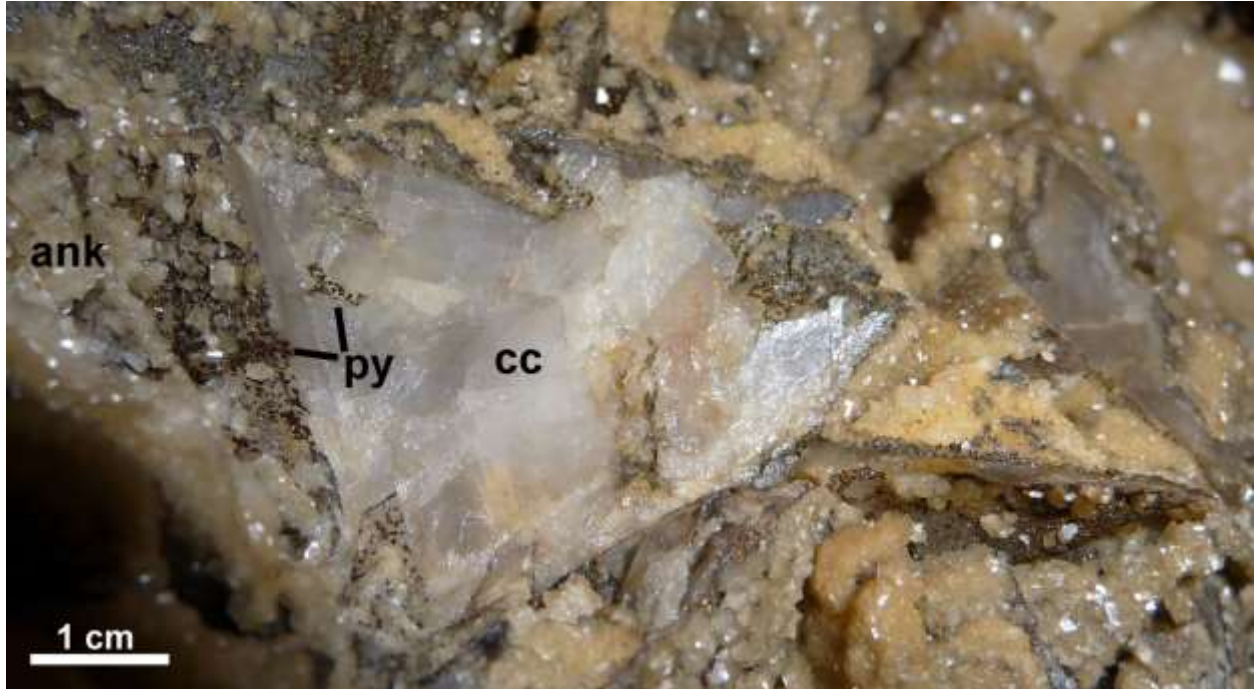

Fig. 7: Late or post-epithermal vein formation stage (VIII), characterized by open space fillings of pyrite (py) and ankerite (ank) ±quartz on, e.g., calcite (cc).

Mineralogy and mineral chemistry of the ore assemblages

The principal ore-forming stages of the paragenetic sequence, as noted above, are stages (II) and (IV). Their intimate spatial association, as well as similar mineral assemblages and textures, suggest that stages (II) and (IV) formed in close succession and are interpreted to be part of the same hydrothermal event. However, the vast majority of the ore phases precipitated early during stage (II). The main Au-bearing phases of this stage are electrum (cf. Mauthner et al., 1996), arsenopyrite and subordinate löllingite. In contrast, the main Ag-bearing phases, besides electrum, are tetrahedrite-group minerals, allargentum and hessite. Positive correlations between As, Sb, Ag and Au, as documented in geochemical assays, as well as trace element analyses show that antimonial arsenopyrite, the dominant As- and Sb-phase in the E-Vein, also hosts Au. This observation is further supported by a sample from the Shaft Vein (Fig. 3), which yielded 89 g/t Au and 114 g/t Ag and consists of quartz and arsenopyrite rimmed by stibnite (Devine, 2008). Electron microprobe compositions of sulfides, sulfosalts and alloys are given in Appendix B.

The principal ore assemblage of electrum + V-mica is commonly associated with quartz, altered K-feldspar and calcite (Fig. 6e and 8). Quartz textures, such as mosaic and plumose, indicate that quartz was originally deposited as amorphous silica or chalcedony (Sander and Black, 1988; Dong

et al., 1995) during ore precipitation. A distinctive feature in the E-Vein is the occurrence of up to ~10 cm nodules of dendritic electrum in V-mica, surrounded by quartz ±calcite, ±K-feldspar, and a thin grey band of arsenopyrite-rich quartz (Fig. 8; Devine, 2012).
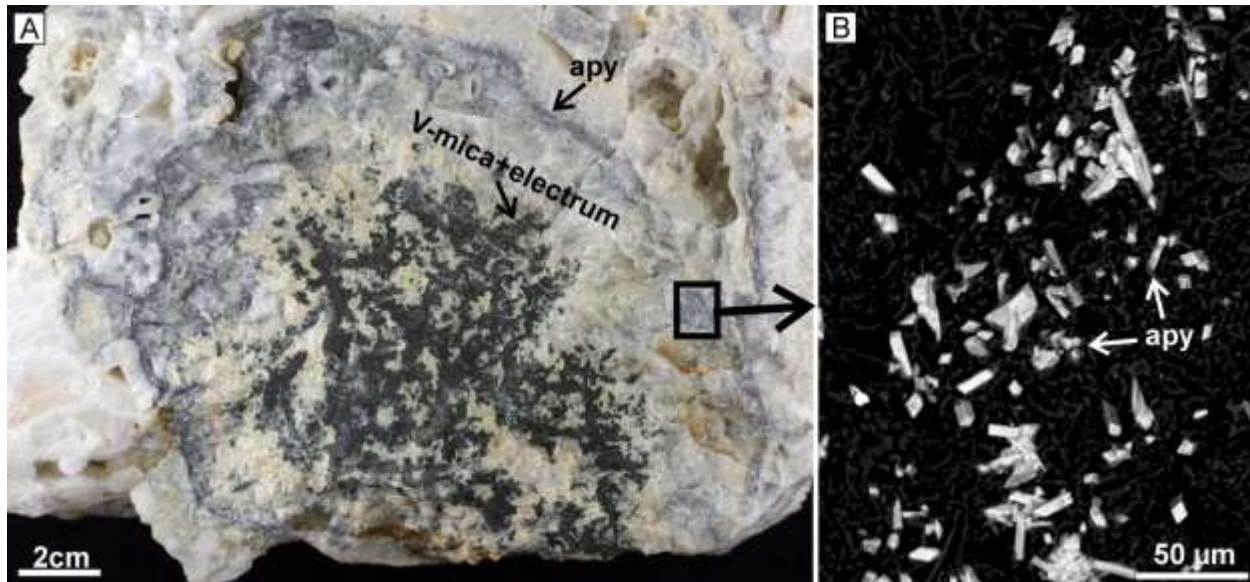

Fig. 8: (A) Nodule of dendritic electrum in dark green V-mica, surrounded by quartz ± calcite and a grey band of arsenopyrite-rich quartz (cf. Devine, 2012). (B) Backscattered electron (BSE) image of acicular arsenopyrite (apy) in quartz.

Stibarsen ('allemontite') has also been reported to be spatially associated with electrum in the E-Vein (Devine, 2008). This paragenesis, however, was not observed during this study, although samples from the heavy mineral concentrate from the 2011 bulk sampling program (Fig. 1) contain abundant fragments of stibarsen. This might be due to the fact that the lower mine levels, which constitute most of the investigated samples, are less 'allemontite'-rich than the upper mine levels (Mauthner et al., 1996).

Electrum (elc)

Electrum is the main Au-bearing phase in the E-Vein and was predominantly formed during stage (II) of the paragenetic sequence. In addition, minor amounts formed during stage (IV). All investigated electrum-bearing samples are from the bulk sample 505-3 (Fig. 1), except for one sample from the 7th mine level (Fig. 9d). Different types of electrum can be distinguished based on textural relationships.

Type I electrum is most prevalent and formed during stage (II) of the paragenetic sequence. Most commonly it forms up to several mm long (irregular) dendrites enclosed in V-mica spherulites (Figs. 9a-c; see also Figs. 6e and 8a). The general order of mineral deposition in this main ore assemblage is electrum, V-mica, K-feldspar + calcite, amorphous silica (Fig. 6e). Less commonly type I electrum may be in contact with, or included in, quartz (Fig. 9d), arsenopyrite/löllingite (Figs. 9e and f), and hessite and/or sphalerite. The Sb- and As-content of type I electrum is generally below detection limit of the EMP (Appendix B1). However, it shows systematic variations in molar

X_{Ag} (Ag/(Ag+Au)) according to its textural position; (1) enclosed in V-mica, hessite, or sphalerite it has X_{Ag} 0.51 to 0.54; (2) in löllingite it has X_{Ag} 0.55 to 0.57, and may contain up to 4.2 wt.% As; (3) in arsenopyrite or quartz it has X_{Ag} 0.56 to 0.57. Furthermore, electrum enclosed in arsenopyrite from the 7th mine level has X_{Ag} 0.58 to 0.62, whereas enclosed in quartz X_{Ag} is 0.56 to 0.57.
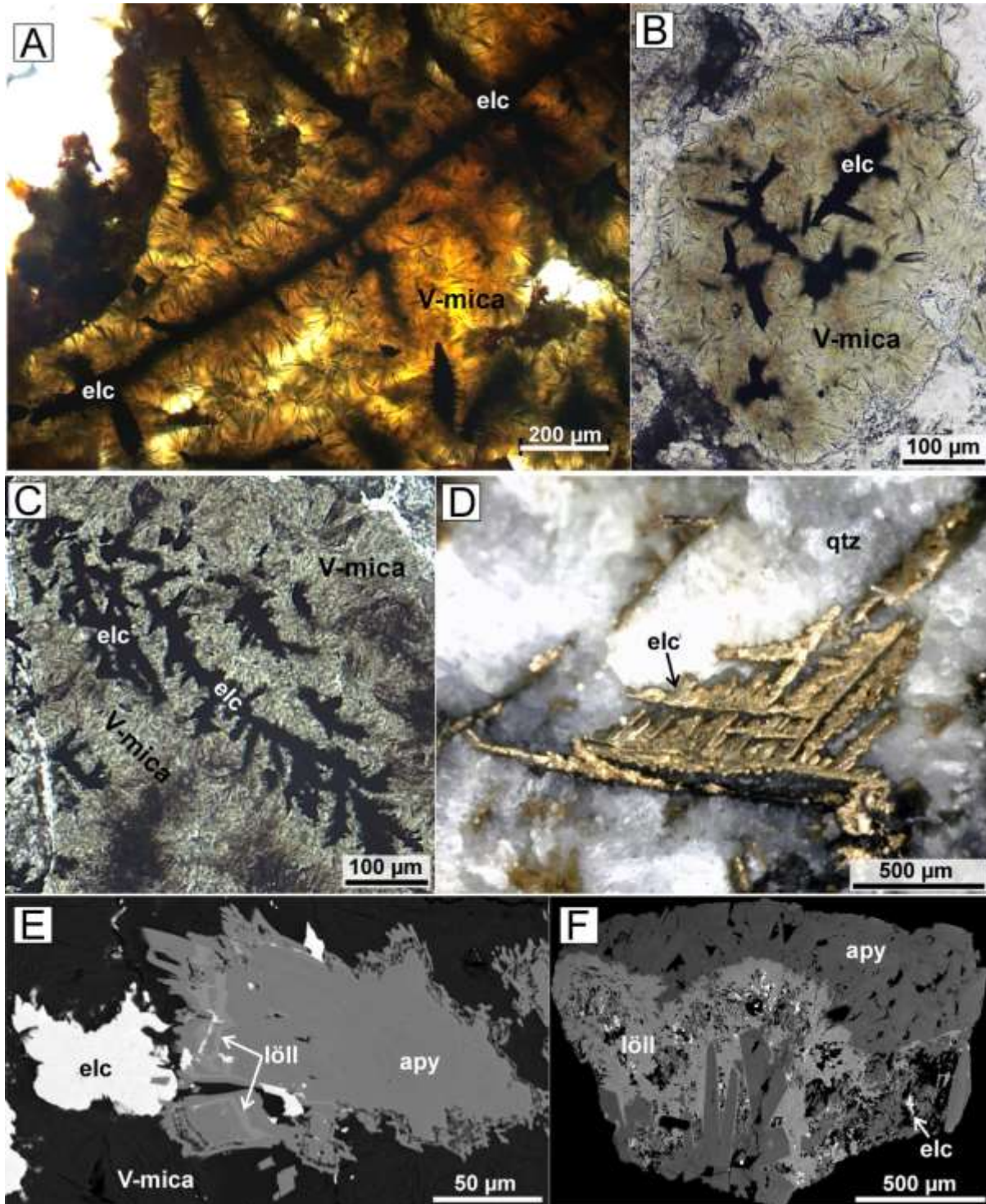

Fig. 9: Photomicrographs of thick (A; 200 µm) and thin sections (B and C), hand specimen image (D), and BSE images (E and F) of type (I) electrum textures and mineral assemblages. (A) Dendritic electrum (elc) enclosed in spherical V-

mica. Plane polarized light (PPL). (B) Short dendrites of electrum in an aggregate of spherical V-mica. PPL. (C) Irregular dendrites of electrum in V-mica. PPL. (D) Coarse-grained dendritic electrum in quartz (qtz) from the 7th mine level. (E) BSE image of electrum associated with interlayered arsenopyrite (apy) and löllingite (löll). The electrum is preferentially associated with löllingite and the arsenopyrite shows skeletal growth. (F) BSE image of electrum in a zone of löllingite between eu- to subhedral arsenopyrite crystals.

Type II electrum, formed during stage (IV) of the paragenetic sequence, is hosted in mosaic-textured quartz, and occurs as individual grains (Fig. 10a), or may be in contact with tetrahedrite-group phases, chalcopyrite and arsenopyrite (Figs. 10b and c), or an Ag-Au-Sb alloy. It is chemically distinct from type I electrum as shown by a markedly higher X_{Ag} of 0.68 (electrum associated with tetrahedrite-group phases), 0.72-0.74 (electrum in quartz), or 0.82 (in contact with Ag-Au-Sb alloy). Furthermore, it may contain up to 2.4 wt% Sb (Appendix B1).
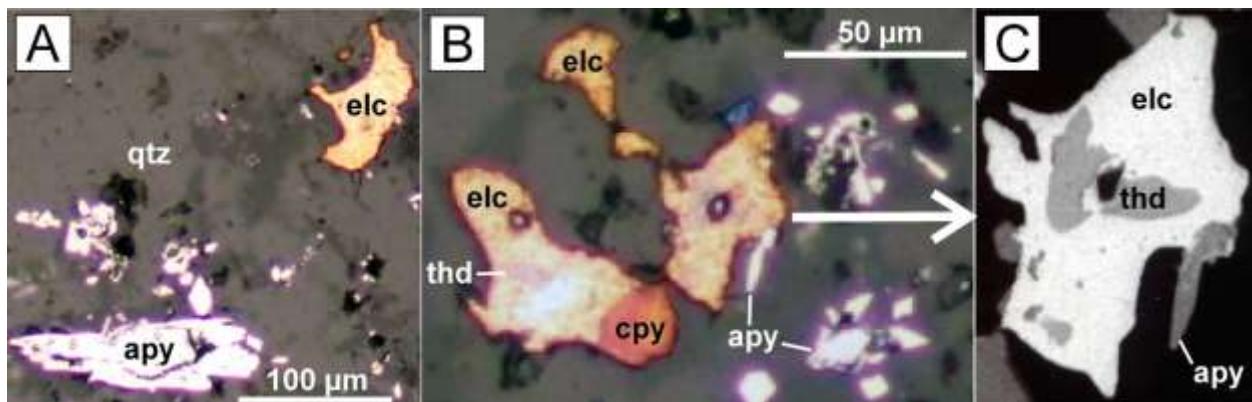

Fig. 10: Type (II) electrum assemblages. (A) Photomicrograph of electrum (elc) and arsenopyrite (apy) in quartz (qtz). Reflected light (RL). (B) Photomicrograph of electrum associated with chalcopyrite (cpy), tetrahedrite-group phases (thd) and arsenopyrite in quartz. RL. (C) BSE of electrum grain with inclusions of tetrahedrite shown in (B).

Arsenopyrite (apy)

Arsenopyrite, after pyrite, is the most common sulfide associated with ore mineralization in the E-Vein. It occurs in a variety of habits, including eu- to anhedral, commonly acicular, up to ~3 mm long prisms (Figs. 8b and 11a), which may form radiating aggregates (Fig. 11a), massive congregations (Fig. 11b), or overgrowths on pyrite (Fig. 11c). In rare instances it includes electrum (Fig. 11b) and may form aggregates consisting of alternating layers of arsenopyrite and löllingite (Figs. 9e-f) (cf. Fig. 62 of Ramdohr, 1980). The arsenopyrite contains between 0.09 and 5.09 wt% Sb (Appendix B2) and may show crystallographically controlled Sb -zonation (Fig. 11e). The antithetic correlation of As with S either indicates the substitution of As for S in arsenopyrite, or the presence of pyrite inclusions (Reich et al., 2005; Fleet and Mumin, 1997), but no correlation between the Sb- and S-, or As-content was observed by Mauthner et al. (1996).
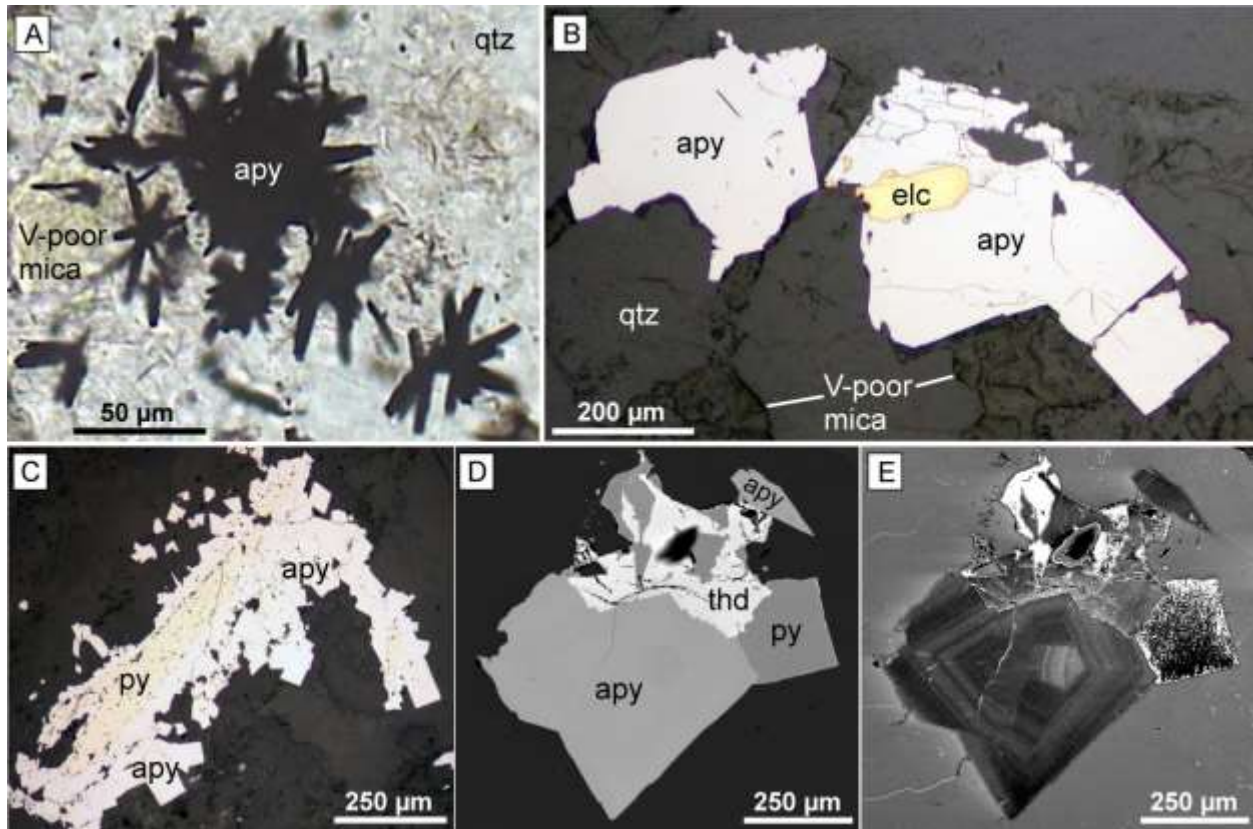
Fig. 11: Photomicrographs (A; PPL) and (B; RL), and BSE images (C), (D) and (E) showing mineral textures and assemblages of arsenopyrite (apy). (A) Radiating clusters of acicular arsenopyrite in quartz (qtz) associated with V-poor mica. (B) Coarse-grained subhedral arsenopyrite with inclusions of electrum (elc) in quartz. (C) Pyrite (py) overgrown by arsenopyrite. (D) Ore assemblage of arsenopyrite, pyrite and a tetrahedrite-group phase (thd). (E) Growth zoning in arsenopyrite crystal shown in (D), highlighted by variable Sb -contents. Image (E) has been modified using the 'Psychedelic' filter of Corel Draw™ in order to highlight chemical zoning.

Löllingite (löll; var. geyerite)

Rare anhedral löllingite is always closely associated with arsenopyrite (cf. Mauthner et al., 1996) and/or electrum (Figs. 9e-f) and may contain up to 4.22 wt% S and 3.34 wt% Au (Appendix B3).

Pyrite (py)

Eu- to anhedral pyrite, up to several mm across is the second most abundant sulfide mineral of the ore-forming stages (II) and (IV), after arsenopyrite. It occurs in contact with all other sulfides, sulfosalts and alloys (Fig. 12), but was not observed in contact with electrum. Based on textural evidence different types of pyrite can be distinguished; (1) porous an- to subhedral pyrite; (2) solid eu- to subhedral pyrite which occurs as single crystals, or surrounds type (1) pyrite; (3) pyrite overgrown by arsenopyrite (Fig. 11c). Type (1) and (2) pyrite may contain inclusions of, or may be intergrown with tetrahedrite-group phases (Figs. 12a and b). No chemical differences were observed among the different types of pyrite (Appendix B4). Pyrite contains up to 5.7 wt% As; the average content, however, is ~0.8 wt% As (n = 91) and values ≥1.3 wt% are interpreted to be due to inclusions of, e.g., arsenopyrite or löllingite. Furthermore, antithetic correlations of As with S

support the presence of these inclusions, or, alternatively may reflect the substitution of As for S in pyrite (Denditius et al., 2008).

Pyrite may show convolute zoning, which is interpreted to document fluid-mineral interaction and accompanying mineral dissolution-precipitation (Fig. 12d; cf. Putnis, 2009). This may also contribute to the observed variations in As-contents.
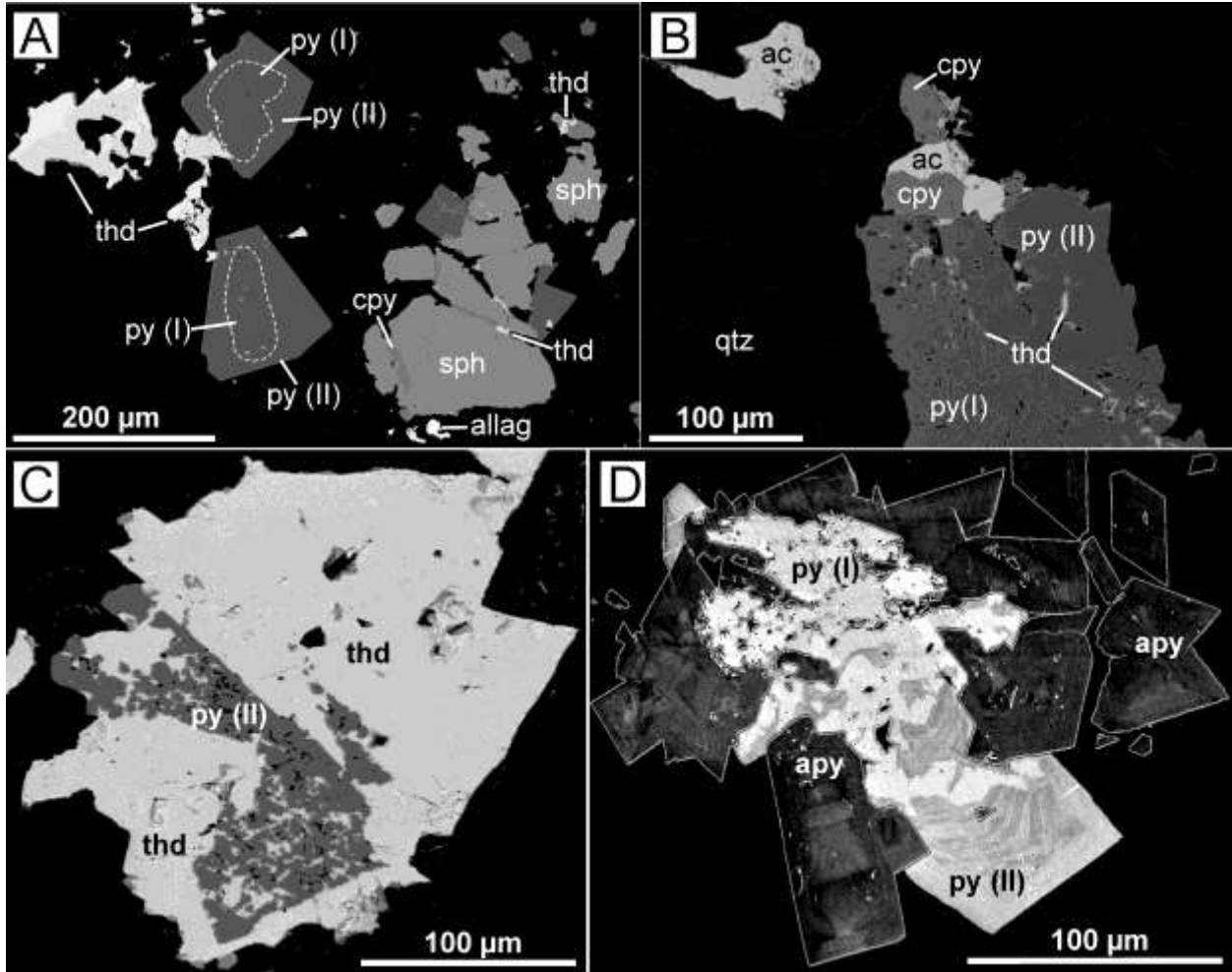

Fig. 12: BSE images of ore assemblages showing the two texturally distinct types of pyrite (py): pyrite (I) is porous and pyrite (II) solid. (A) The assemblage tetrahedrite-group (thd), pyrite(I), pyrite(II), allargentum (allag) and sphalerite (sph). (B) The assemblage pyrite (I), pyrite(II), tetrahedrite-group, chalcopyrite (cpy), acanthite (ac). (C) Pyrite (II) intergrown with a tetrahedrite-group mineral. (D) The convolute and erratic zoning in pyrite (I) and (II) is interpreted to reflect mineral-fluid interaction and accompanying mineral dissolution-precipitation. In contrast, arsenopyrite (apy) shows crystal growth zoning. The BSE image (D) has been modified using the 'Psychedelic' filter of Corel Draw™ in order to highlight chemical zoning.

Chalcopyrite (cpy)

Anhedral chalcopyrite is a minor constituent of the ore assemblage and occurs as single grains, or is associated with pyrite or sphalerite, and less commonly with type (II) electrum (Fig. 10 b). Its chemical composition corresponds to the ideal stoichiometry (Appendix B5).

Sphalerite (sph)

Sub- to anhedral sphalerite is a minor constituent of the ore assemblage and characteristically is associated with hessite, electrum and V-mica (Fig. 13). In rare instances it shows a chemical zonation from Fe-rich core (~3.8 wt%) to Fe- poor rim (~2.6 wt; Fig. 13a). The Cd-content of the analyzed sphalerite ranges from 0.4 to 0.8 wt% (Appendix B6), and the molar X_{Fe} (Fe/(Fe+Zn)*100) varies between 4.0 and 10.1 (average = 5.1; n = 48). In contrast, sphalerite enclosed in pyrite, which is interpreted to not be part of the ore-forming stages has a higher X_{Fe} of 9.3 to 19.3 (average = 14.4; n = 8).
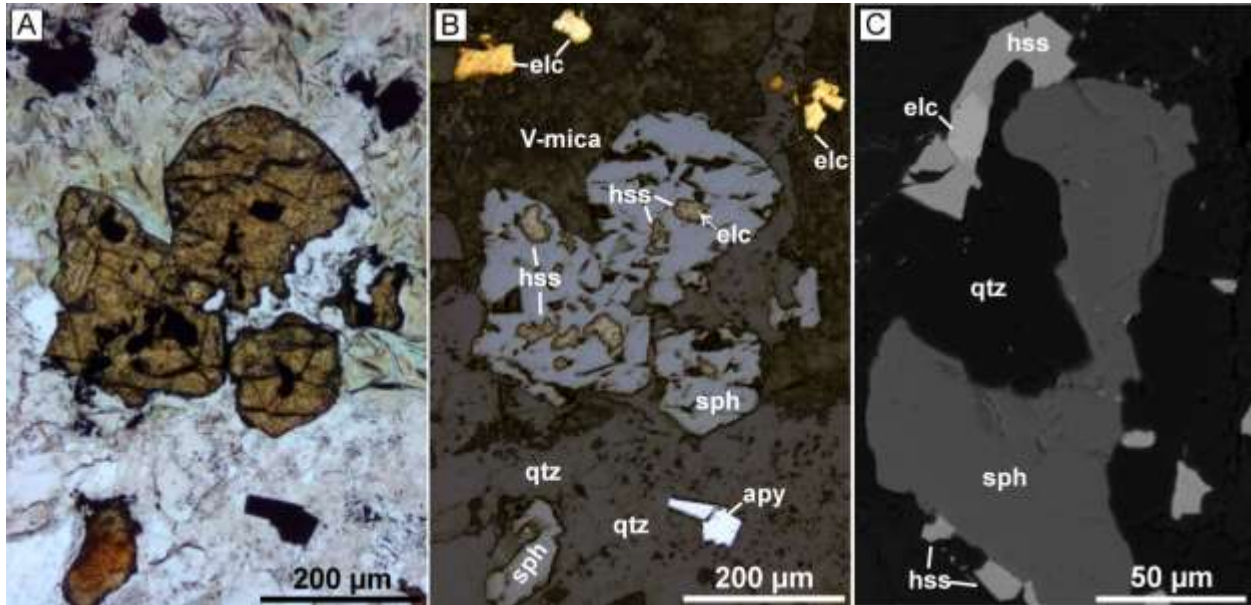

Fig. 13: Photomicrographs (A; PPL) and (B; RL), and BSE image (C) of the assemblage V-mica, electrum (elc), sphalerite (sph), hessite (hss) and arsenopyrite (apy). The sphalerite grain in the lower left of (A) shows a zonation from Fe-rich core to Fe-poor rim. Hessite in (B) and (C) contains microinclusions of electrum.

Hessite (hss)

Rare anhedral, up to ~30 μm hessite is intimately associated with sphalerite and/or electrum (Fig. 13), except for one sample where it occurs in contact with pyrite and arsenopyrite. The chemical composition of the hessite commonly corresponds to the ideal stoichiometry, but in rare cases it contains up to 0.5 wt% S (Appendix B7).

Tetrahedrite-group phases (thd)

Anhedral, up to ~200 μm tetrahedrite-group minerals are a minor constituent of the ore assemblage that formed predominately during stage (II) and, to a lesser degree during stage (IV) of the paragenetic sequence. Those formed during stage (II) commonly occur as inclusions in, or intergrown with, pyrite (Figs. 12b and c), or are closely associated with arsenopyrite, pyrite, chalcopyrite, sphalerite and allargentum (Figs. 11d and 12a). In contrast, tetrahedrite-group phases that formed during stage (IV) are present as inclusions in type II electrum (Fig. 10c), or are in contact with an AgAuSb alloy. In both cases the tetrahedrite-group minerals are Ag-rich (Appendix B8; Fig. 14) with up to 7.7 a.p.f.u. (38. 3 wt%) Ag and are accordingly classified as Ag-rich

tetrahedrite (Ag <4 a.p.f.u.), freibergite (Ag ~6 a.p.f.u.), or argentotetrahedrite (Ag >6 a.p.f.u.) (Moelo et al., 2008).
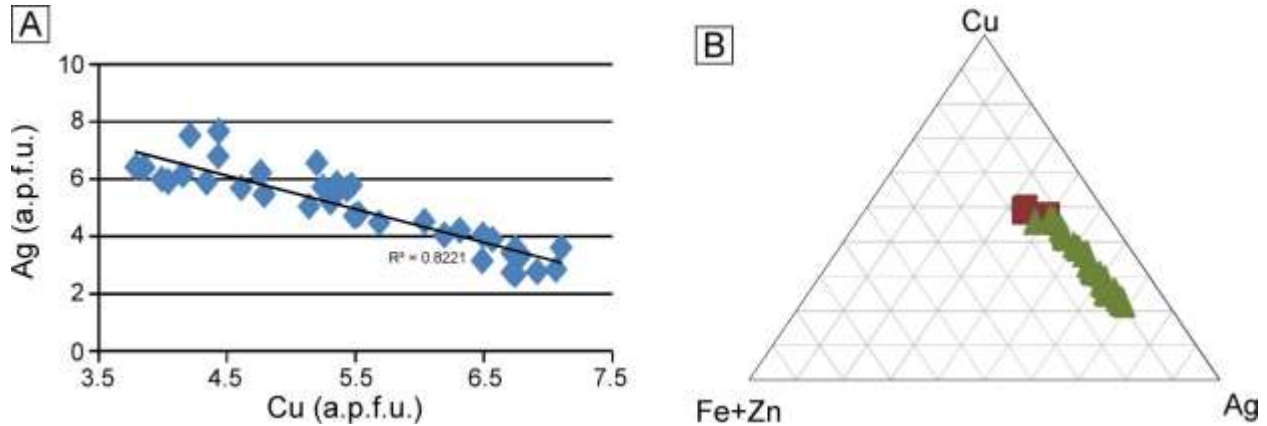

Fig. 14: Diagramatic representation of the compositional range of tetrahedrite-group minerals from the Engineer and Double Decker Veins plotted as (A) Cu versus Ag in atoms per formula unit (a.p.f.u.) and (B) in (Fe+Zn)-Cu-Ag space. Green triangles = E-Vein; red squares = DD-Vein.

Allargentum (allg; $Ag_{1-x}Sb_x$; x = 0.09-0.16)

Anhedral allargentum occurs in trace amounts and formed during stages (II) and (IV) of the paragenetic sequence. Two varieties of allargentum can be distinguished. Type (1) formed during stage (II) and commonly occurs in association with unidentified sulfide and/or tetrahedrite-group minerals. Based on textural evidence it cannot be unambiguously determined if some of this allargentum formed by the breakdown of Ag-rich tetrahedrite. In contrast, type (2) allargentum formed during stage (IV) and is associated with mosaic quartz. Type (1) may contain up to 0.8 wt% Cu, but this may be an analytical artifact due to its small grain size and its association with Cu-bearing phases. In all other respects the two types are chemically similar and correspond to the stoichiometric formula (Petruk et al., 1970; Appendix B9). The Hg-content of the analyzed allargentum is below detection limit and it contains up to ~2 wt% S. Wether this sulfur is due to tarnishing of the samples (cf. Staude et al., 2007) or is incorporated in the crystal structure could not be determined during this study and needs further investigation.

Dyscrasite (dys; $Ag_{3+x}Sb_{1-x}$; x ≤ 0.2)

Anhedral dyscrasite was encountered as a trace mineral in one sample in association with pyrite, arsenopyrite and tetrahedrite-group phases. The totals (n = 5) shown in Appendix B10 exceed 101 wt% for unknown reasons. However, the calculated mineral formulae correspond to the ideal stoichiometry and the analyses are interpreted to closely reflect the true composition of dyscrasite from the Engineer Vein.

Galena (PbS)

Very fine-grained galena occurs as a trace mineral in V-bearing mica. Due to its fine grain size (<3-5 μm) and inclusion in mica its presence could only be inferred by EDX spectroscopy and no quantitative analysis was possible.

Stibarsen ('Allemontite') and native arsenic:

The Engineer Mine is a Dana locality for 'allemontite' (discredited species; stibarsen + native arsenic; Ramdohr, 1980; Mauthner et al., 1996) and botryoidal masses up to 30 cm in size have been reported (Mauthner et al., 1996). According to Ramdohr (1960), this botryoidal habit points to the crystallization of a gel. However, aggregates of arsenic crystals, each up to 1 mm across, have also been described (Mauthner et al., 1996), but were not observed during this study. The specimens investigated during this study were recovered from the heavy mineral concentrate from the 5th mine level bulk samples (Fig. 1) and represent fragments of larger botryoidal masses. Individual fragments show a wide variety of internal textures (Figs. 15a-c), resembling those caused by the undercooling and solidification of alloys. The chemical compositions of individual domains or layers range from 9.8 to 95.5 wt% As, and 4.5 to 87.2 wt% Sb (Fig. 15d; Appendix B11). However, the Sb-content commonly does not exceed ~62 wt%, which corresponds to stoichiometric AsSb.
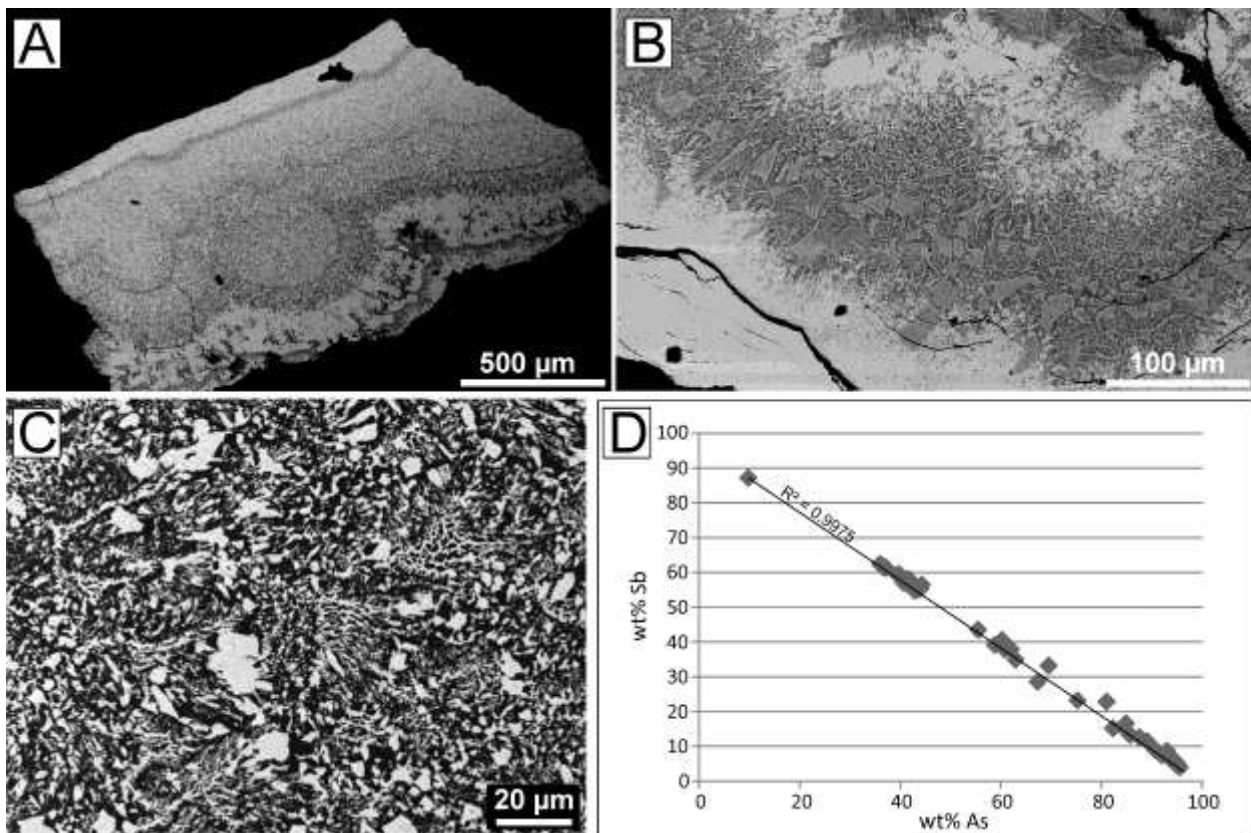
Fig. 15: BSE images of macro- and microscopic stibarsen textures (A, B and C) and chemical compositions of individual stibarsen domains (D). Sb-rich layers/domains in (A), (B), and (C) are characterized by a lighter grey tone, compared to darker As-rich layers/domains. (A) and (B) Colloform to spherical layering of Sb- and As-rich layers in stibarsen. (B) and (C) Microtextures in stibarsen resembling textures produced by solidification of an undercooled alloy melt (see section X). (D) The chemical composition of individual 'stibarsen' domains ranges mostly from ~62 wt% Sb, i.e., stoichiometric stibarsen (SbAs), to <5 wt% Sb, i.e., close to native arsenic.

Acanthite (Ag_2S)

Rare Sb-rich acanthite occurs as anhedral grains in the vicinity of, or in contact with, pyrite, chalcopyrite and a tetrahedrite-group phase, or in an assemblage with pyrite, chalcopyrite,

arsenopyrite, tetrahedrite-group phase and allargentum. Acanthite contains on average (n = 11) 12.6 wt% Sb, ~0.1 wt% Fe,~0.1 wt% Cu, and As is below detetection limit (Appendix B12).

Unidentified Phases X1 and X2

Two accessory phases have been encountered during this study that could not be unambiguously identified. The textural settings and mineral chemistries of these phases, referred to as X1 and X2, are presented in Figure 16 and Appendices B13 and B14, respectively.

X1 - $(Cu_{2.30}Fe_{2.28}Ag_{0.52})S_{4.89}$

Phase X1 with the empirical formula $(Cu_{2.30}Fe_{2.28}Ag_{0.52})S_{4.89}$ (average of 9 analyses normalized to 10 ions; Appendix B13) was observed in contact with tetrahedrite-group phases (Fig. 16a) and as a rim around allargentum (Fig. 16b). The Zn-, As-, Sb- and Hg-contents of this phase are below detection limit, and the totals are between 95.5 and 98.3 wt% (avg. = 96.8 wt%; n = 9). The low totals can have several reasons; (1) one or more elements contained in this phase were not analyzed for, (2) the analyzed surfaces were uneven, or (3) certain elements were mobilized during analysis due to beam damage. However, the above empirical formula is considered a good first approximation, because it is in agreement with the formulae obtained from individual analyses with totals of ≥97 wt.%, and it has an almost neutral charge (-0.09). Furthermore, EDX spectroscopy did not reveal any other element than those that have been analyzed for. Based on textural observations we interpret this phase to be of primary origin, but we caution that our results and interpretations are preliminary and that this phase needs to be addressed in detail in a separate study.

X2 – $Ag_{1.53}Sb_{0.23}Au_{0.14}S_{0.10}$

Phase X2 with the empirical formula $Ag_{1.53}Sb_{0.23}Au_{0.14}S_{0.10}$ (average of 5 analyses normalized to 2 ions; Appendix B14) occurs in association with type (II) electrum and a tetrahedrite-group phase (Fig. 16c and d). Its texture, as revealed by BSE imaging (Fig. 16d), suggests an intimate intergrowth of two phases with relatively small differences in their Ag-, Sb-, Au-, and/or S-contents, or the decomposition of a single precursor phase. The As-content of X2 is below the detection limit of 0.29 wt%. Based on textural evidence we interpret this phase, or its precursor phase in the case of decomposition, to be of primary origin. However, as with X1, a more exhaustive examination is needed to fully understand and describe this phase.
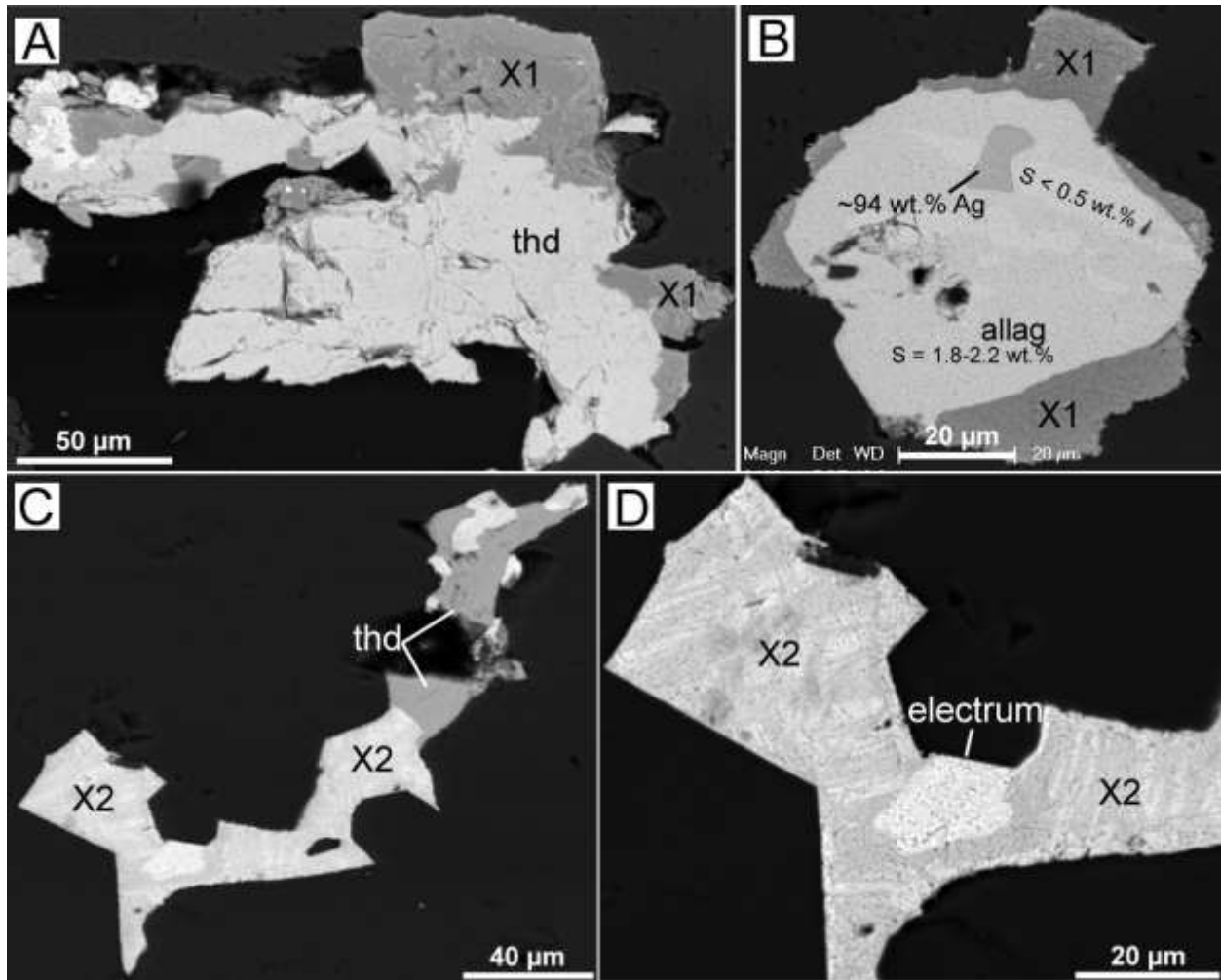
Fig. 16: BSE images showing the textural positions of the unidentified phases X1 (A and B) and X2 (C and D). The empirical mineral formulae, based on averaged chemical compositions, are X1 = $(Cu_{2.30}Fe_{2.28}Ag_{0.52})S_{4.89}$ and X2 = $Ag_{1.53}Sb_{0.23}Au_{0.14}S_{0.10}$.

Mineralogy and mineral textures of gangue phases

The distribution of the dominant gangue phases in veins of the 5th mine level have been mapped by Devine (2008) (Fig. 3), and those of the Engineer Vein on the 6th and 7th mine level by Coates (2012). The dominant gangue phases in decreasing order are quartz, carbonate, muscovite (Devine, 2008). These phases likely crystallized during multiple stages of the paragenetic sequence. For the purpose of this study, however, we focus on gangue phases of the Engineer Vein that developed during and between the ore-forming stages (II) and (IV).

Quartz (qtz)

Quartz is the most abundant gangue phase and shows a variety of macro- and microscopic textures. In late vein stages open space textures, such as comb quartz, predominate. In contrast, during the ore-forming stages (II) to (IV) amorphous silica or chalcedony (Fig. 6c) precipitated and subsequently recrystallized to quartz for the most part. Macroscopically, quartz of these stages forms characteristic colloform-crustiform, and cockade textures (Dong et al., 1995; Fig. 6), but may

28

also be massive in appearance. Microscopically, quartz is commonly inequigranular on a thin section scale and the recrystallization of amorphous silica to quartz is reflected in the following textures (cf. Adams, 1920; Lovering, 1972; Sander and Black, 1988; Dong et al., 1995): The most typical quartz textures associated with ore-mineralization in the investigated samples are mosaic (Fig. 17a) and plumose (Figs. 17a-d). In addition, zonal (Figs. 17c-f) and moss texture quartz, as well as replacement textures such as quartz after platy (Figs. 17f and 6a) or rhombic calcite (Figs. 18e) have been observed. Furthermore, the common association of plumose and (in-)equigranular interlobate to polygonal quartz is interpreted to indicate the advanced recrystallization of formerly mosaic (jigsaw) textured quartz due to static recrystallization.
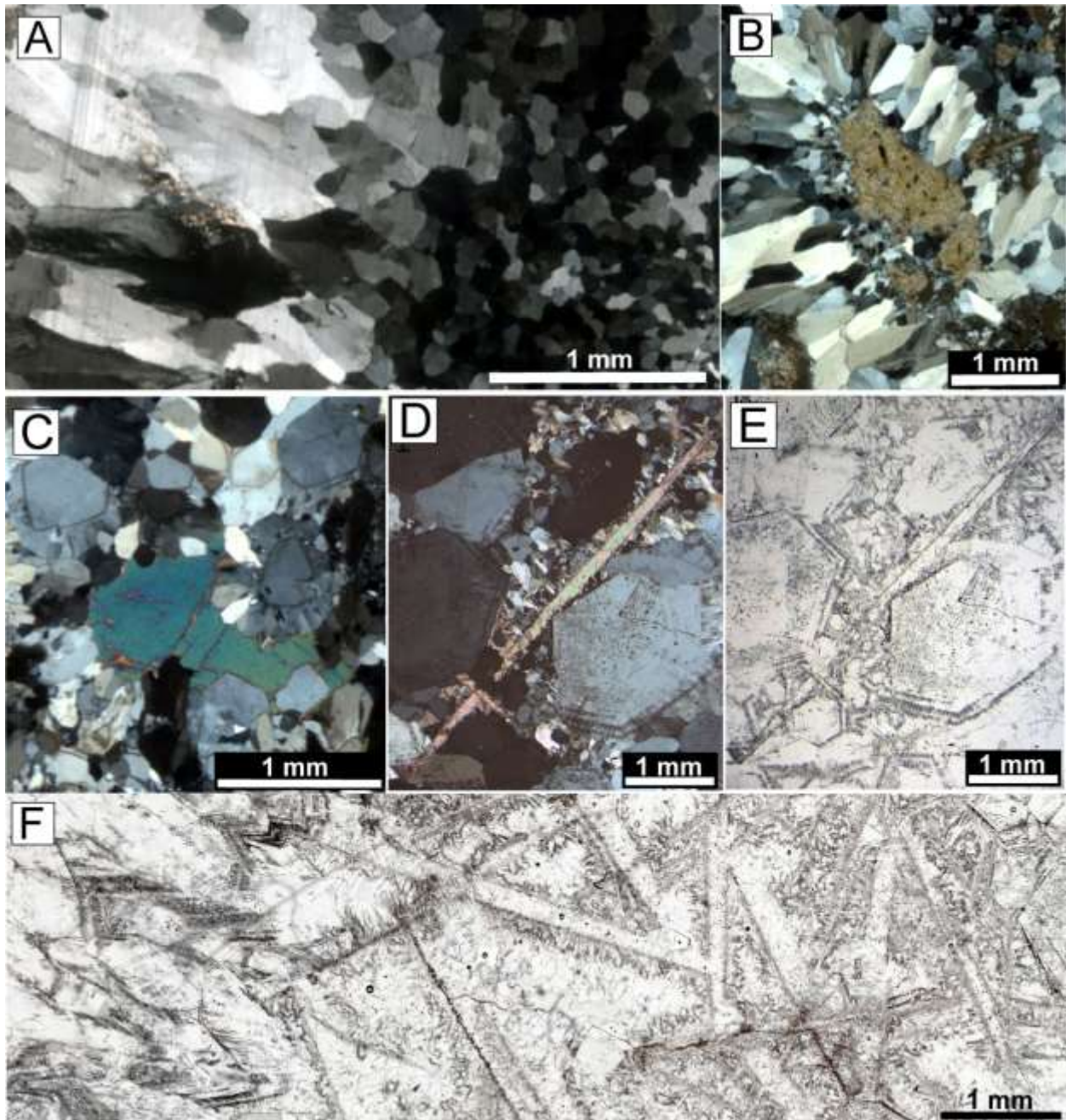
Fig. 17. Photomicrographs of quartz textures related to the ore forming stages (II) and (IV). Mosaic (A) and plumose quartz textures (A to E) indicate the recrystallization of amorphous silica or chalcedony. (A) Mosaic textured quartz grades into plumose (feathery) quartz. XPL. See figure 6d for overview. (B) V-mica (orange-green; center of image) includes electrum (black spots) and is surrounded by radiating crystals of plumose quartz. XPL. This texture is interpreted to indicate that this quartz was originally deposited as amorphous silica enclosing the other phases. (C) Zones of plumose quartz surrounding euhedral quartz cores with growth zones. However, in some cases the plumose quartz crosses these growth zones and some zones have rounded outlines. This is interpreted to indicate that also the core zones may have been formed by substantial recrystallization of amorphous silica or chalcedony (cf. Sander and Black, 1988). XPL. (D) Zones of plumose quartz crossing quartz growth zones. Textural evidence indicates that the delicate platy (bladed) calcite crystals in the center of the image grew together with the surrounding quartz. XPL. (E) Same as (D), but in PPL, highlighting growth zones in quartz. (F) Zonal quartz at the left-hand side of the image is intergrown with lattice bladed quartz, which replaced earlier platy calcite.

Calcite (cc)

Calcite is the second most abundant gangue phase after quartz and occurs as massive aggregates and eu- to subhedral platy (Figs. 18a-d; see also Fig. 4c) or rhombic crystals (Figs. 18d-g), both of which can have been replaced by quartz (Figs. 17f and 18e; cf. Mauthner et al., 1996). For the purpose of this study we focus on rhombic and platy calcite related to the ore-forming stages (II) to (IV). Rhombic and platy calcite occur either spatially separated, or in close association (Figs. 18d and 4c). In general, the occurrence of platy calcite in the geothermal environment is interpreted to result from boiling of the hydrothermal fluid and its growth rate was estimated to be ~0.1 mm/day for New Zealand geothermal systems (Tulloch, 1982; in Simmons and Christenson, 1994). However, the close association of rhombic and platy calcite observed in some samples indicates that both crystal habits can develop simultaneously. The observation that platy calcite crystals preferentially occur close to the vein center (Figs. 4c and 6a), nevertheless, suggests that uninhibited crystal growth favors, or is mandatory for, the development of the platy habit. Although this is in agreement with the precipitation of platy calcite in open spaces, as observed by Simmons and Christenson (1994), it does not exclude the possibility that platy calcite may form in a (silica) gel suspension, as suggested by the association of platy calcite and plumose quartz (Fig. 17d). Furthermore, platy calcite usually occurs as single crystals showing homogenous extinction (Fig. 18b), but in rare cases it can be composed of numerous sub grains (Fig. 18c). How this particular texture forms, and if it represents a primary or secondary feature could not be unambiguously determined. Moreover, mosaic and plumose textures, indicative of the recrystallization of amorphous silica to quartz (Fig. 18i), have also been observed in calcite (Fig. 18h) and suggest that this calcite may have in parts been originally deposited as amorphous calcium carbonate (ACC). This interpretation is supported by textures that document the mutual development of euhedral crystal habits of adjacent quartz and calcite (Fig. 18g), interpreted to indicate their simultaneous precipitation in presumably amorphous form and subsequent recrystallization, as indicated by plumose quartz.
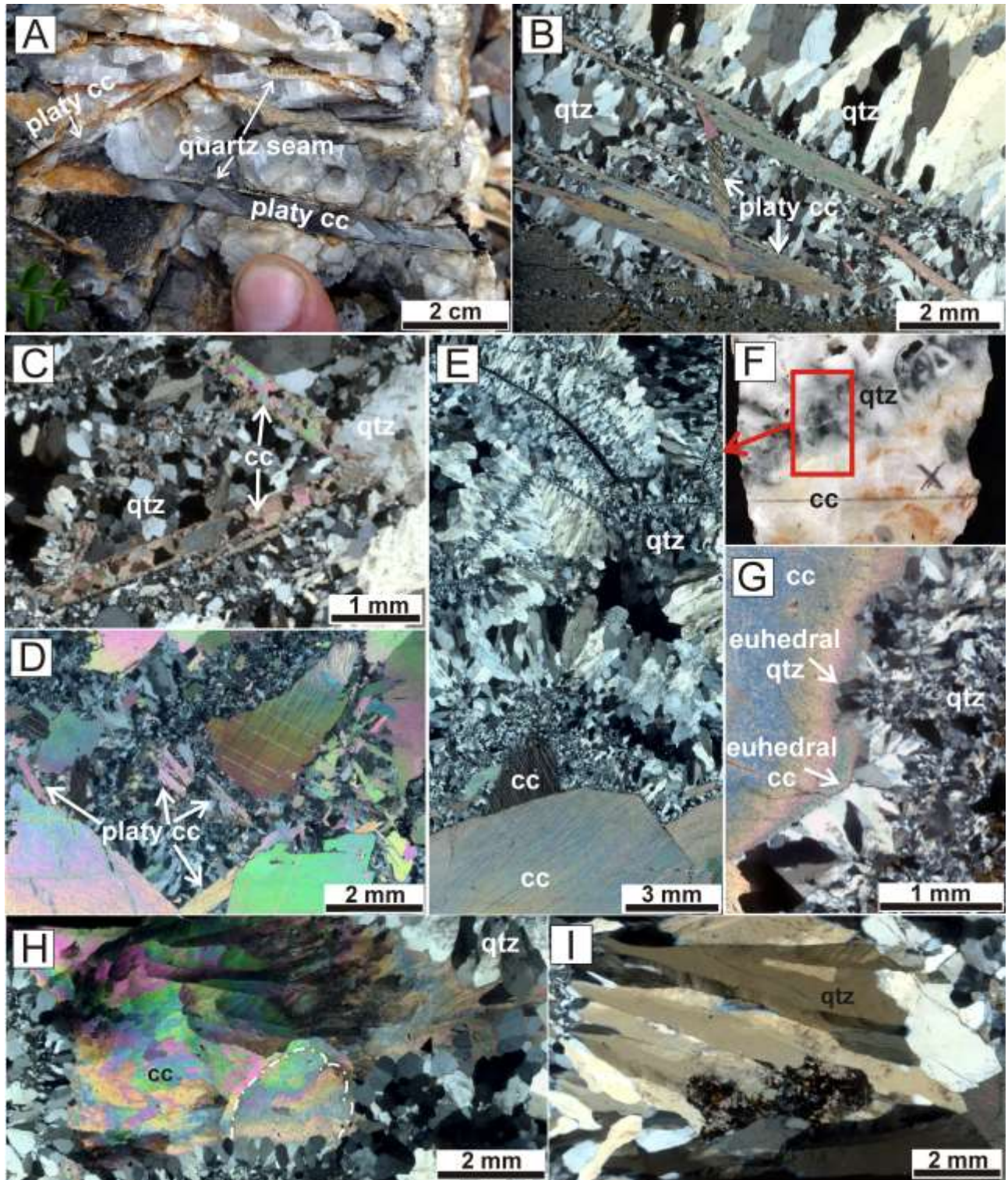
Fig. 18. Field (A) and sample image (F), as well as photomicrographs (B) to (E) and (G) to (H) of calcite habits and textures formed during ore formation. (A) Platy calcite (cc) rimmed by thin seams of quartz. Interstices have been filled by a second generation of calcite. (B) Platy calcite associated with mosaic and plumose quartz. XPL. (C) Platy calcite crystals composed of multiple sub-grains in a matrix of mosaic and plumose quartz. XPL. (D) Co-existing and partly intergrown platy and rhombic calcite crystals. Furthermore, the rhombic calcite crystal in the center right shows deformational features on its upper tip. XPL. (E) In the upper part of the image the outlines of rhombic calcite that has been replaced by quartz are visible. XPL. (F) Sample image of detail shown in (E). The replacement of rhombic calcite

by quartz also created abundant vugs. (G) The mutual development of euhedral crystal habits of adjacent quartz and calcite is interpreted to indicate their simultaneous precipitation in amorphous form, as indicated by plumose quartz textures (see text), and their subsequent recrystallization. XPL. (H) The mosaic and plumose textures in calcite resemble those observed in quartz (cf. 18I) and are interpreted to indicate that carbonate was in parts originally precipitated in amorphous form. XPL. Note also the spherical outline preserved in calcite (stippled white line). (I) Plumose quartz textures, similar to the calcite textures shown in 18H, are indicative of the recrystallization of amorphous silica to quartz. XPL.

K-feldspar (kfs)

In the epithermal veins of the Engineer Mine cream-colored to orange, eu- to anhedral fine grained K-feldspar occurs as an accessory gangue phase closely associated with the main ore assemblage V-mica + electrum + (recrystallized) quartz (Fig. 6e). All observed K-feldspar was intimately intergrown with calcite, as well as subordinate Fe-oxides, phyllosilicates and quartz (Fig. 19). Due to the fine grain size and the intimate intergrowth of this assemblage not all phases could be unambiguously determined. Furthermore, the two main phases of this assemblage, i.e. K-feldspar and calcite, both show homogenous extinction (Fig. 19b). This could indicate that K-feldspar and calcite grew simultaneously as intergrown single crystals. Alternatively, one phase, presumably K-feldspar, is being replaced by the other, and, for an unknown reason, the replacing phase behaves optically as a single crystal. Given their different crystal systems and chemical compositions we regard the second possibility as more likely.
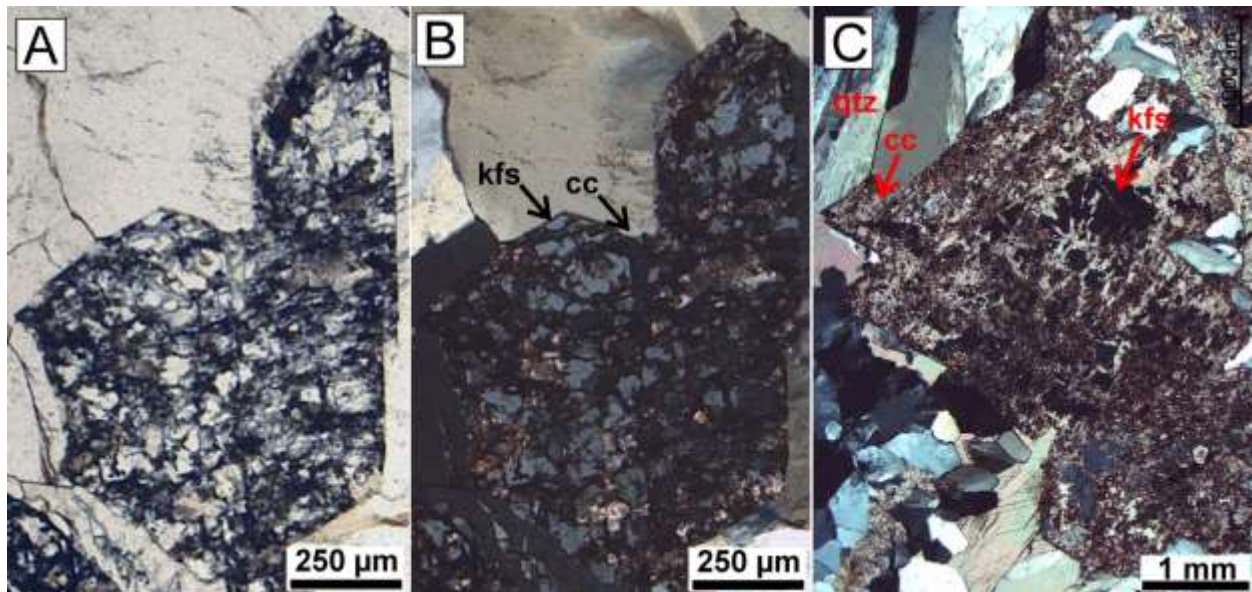
Fig. 19. Photomicrographs of K-feldspar/adularia-calcite intergrowths related to the main ore forming stage (II). See also Figure 6e. (A) Intergrowth of euhedral K-feldspar (kfs) and calcite (cc). PPL. (B) same as (A), but in XPL. Notably, K-feldspar, as well as calcite (black; in extinction) show homogenous extinction. (C) K-feldspar (black) intergrown with calcite in an assemblage with V-mica (top right) and plumose quartz (top and bottom left). K-feldspar as well as calcite show homogenous extinction. XPL.

(V-)mica

Dark to light green, an- to subhedral mica is a common accessory gangue phase in epithermal veins of the Engineer mine. The dark green mica, referred to as type (I), is characteristic for the main ore forming stage (II) (Figs. 6c-e), contains up to ~11 wt% vanadium (Appendix B15), and typically occurs as spherical concretions up to 10 cm in diameter, closely associated with sulfides, sulfosalts, alloys and K-feldspar (Figs. 6e and 20a). These concretions frequently contain electrum in the center (Figs. 9a-c, and 6e), and may show a zonation of V-rich core to V-poor rim (Fig. 20f; cf. Devine, 2012). Type (I) mica is fine to coarse grained and grey-brown to pale green in thin section (Fig. 20d), respectively.

In contrast, light green mica, type (II), formed during stage (IV) and possibly subsequent stages of the paragenetic sequence (Figs. 6a and c-d), has <0.8 wt% vanadium, and may or may not be associated with ore phases. Notably it was not observed in association with electrum. Type (II) mica is grey-brown in color (PPL), typically finer grained than type (I) mica and commonly forms layers, or irregular masses composed of very fine grained and intimately intergrown mica and quartz. Both mica varieties develop similar characteristic textural features, such as spherical and vermicular concretions (Fig. 20a-f), and are exclusively associated with recrystallized quartz. Notably, the spherical concretions frequently display textures similar to recrystallized quartz (Fig. 20a), as for example described by Herrington and Wilkinson (1993) from mesothermal vein systems. Alternatively, this texture may represent the primary growth texture of V-mica spherules, similar to textures observed by Keith and Padden (1964). Furthermore, the vermicular structures formed by type (II) mica commonly contain a central dark band consisting of minute arsenopyrite ± galena ± Ca-bearing phase (Fig. 20b). Due to its fine grain size, however, this assemblage could usually not be unambiguously determined, but in rare cases the arsenopyrite crystals are of sufficient size to be clearly identified (Fig. 20c). The above textural observations indicate that type (I) and (II) mica precipitated under similar hydrothermal conditions, possibly in amorphous form and together with amorphous silica or chalcedony.
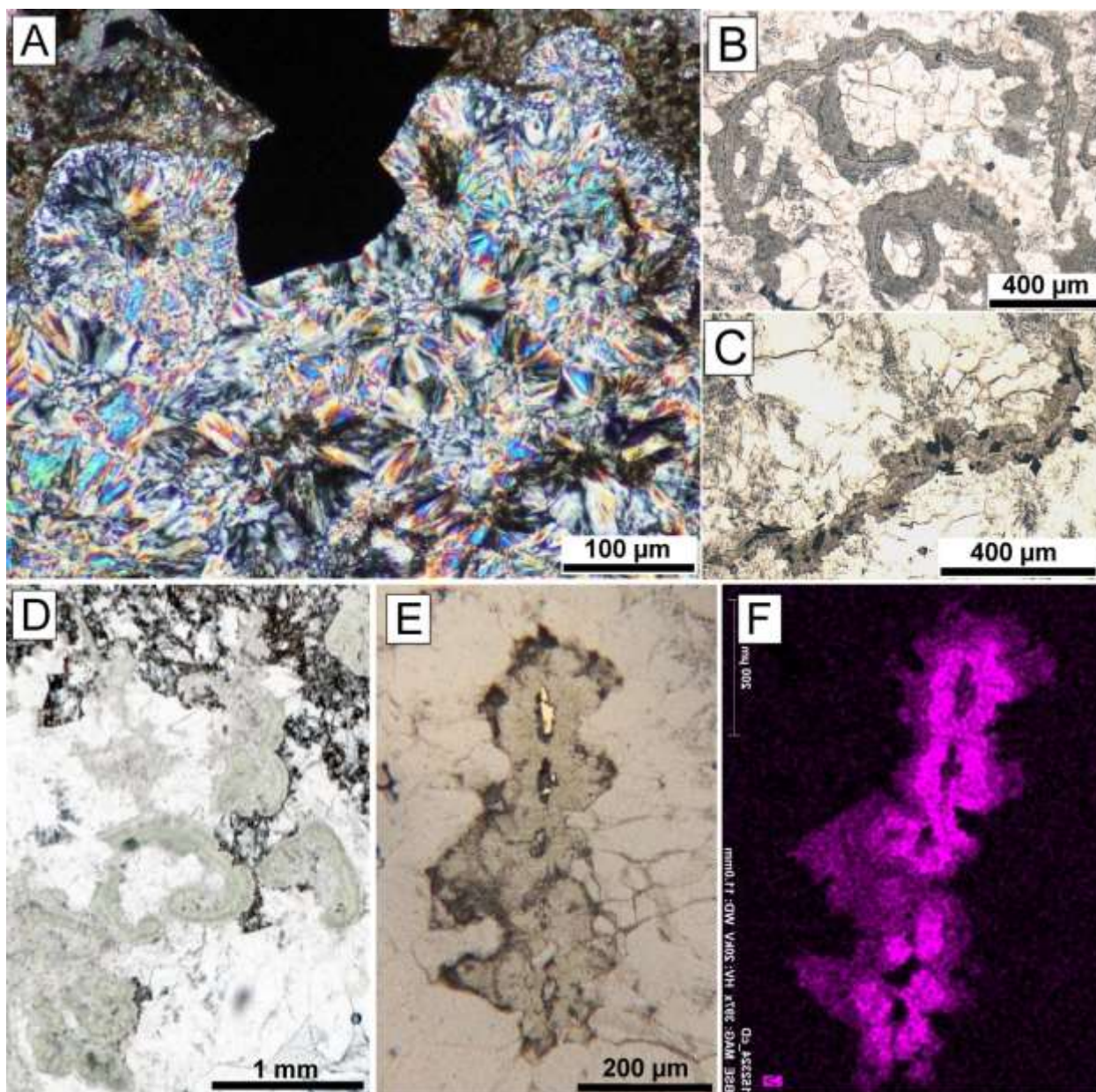
Fig. 20. Photomicrographs (A to E) of V-mica textures, and element map (F) of the vanadium distribution in V-mica enclosing electrum. (A) Aggregate of type (I) V-mica spherules showing polygonal grain boundaries, presumably due to recrystallization of an amorphous precursor (see text). XPL. (B) Vermicular type (II) mica with central bands of arsenopyrite ± galena ± Ca-phase. PPL. (C) Similar to (B), but with coarser grained, mostly central crystals of arsenopyrite. PPL. (D) Type (II) V-mica in association with K-feldspar-calcite (top of image) and plumose quartz (white). PPL. See Figure 6e for reference. (E) Aggregate of spherical Type (II) V-mica with central electrum. RL. (F) EDX element map of (E), showing that the highest V-concentration in V-mica is found in the central part in proximity to electrum.

Based on chemical analyses (Appendix B15), all analyzed micas are classified as interlayer-deficient micas of the illite series (positive interlayer charge x ≥0.6 and <0.85; Rieder et al., 1998; Guggenheim et al., 2006). The compositional ranges of vanadian illite from the Engineer Vein are similar to those reported for V-rich muscovite and roscoelite from the Hemlo Gold deposit, Ontario,

Canada (Fig. 21a). Furthermore, the negative correlation between V^{3+} and Al^{3+} in the octahedral positions suggests the direct substitution of these elements (Fig. 21b) (Pan and Fleet, 1992).
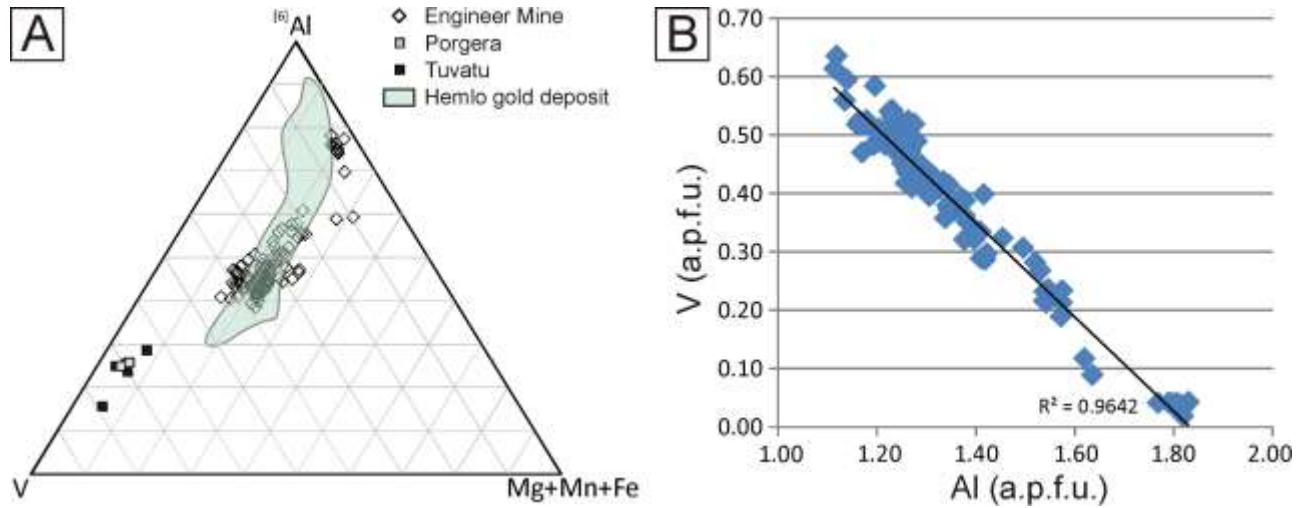

Fig. 21. (A) Chemical compositions of V-illite from the Engineer Mine and V-rich muscovite and roscoelite from the Hemlo Gold deposit (Pan and Fleet, 1992), the Porgera gold deposit (Ronacher et al., 2002) and the Tuvatu gold-silver prospect (Spry and Scherbarth, 2005) shown in the $^{[6]}$Al-V-(Mg+Mn+Fe^{2+}) ternary diagram. (B) The substitution of V^{3+} for Al^{3+} in the mica crystal structure is indicated by the negative correlation between V and Al.

Trace element analysis

In-situ trace element analyses of pyrite, pyrrhotite, arsenopyrite, chalcopyrite, sphalerite, tetrahedrite, löllingite, stibarsen, hessite and electrum were conducted via LA-ICPMS (Figs. 22 and 23). A total of 30 elements (Al, Si, S, Ca, Ti, V, Cr, Mn, Fe, Co, Ni, Cu, Zn, As, Se, Y, Zr, Mo, Ag, Cd, Sb, Te, Ba, Ce, Ta, Re, Au, Tl, Pb, Bi) have been analyzed. The following discussion, however, will focus on the Au-content of the investigated phases. The average Au-contents of the analyzed phases are shown in Table 2.

The trace element analyses show that at the Engineer Mine property arsenopyrite is the most significant ore phase besides electrum due to its Au-content and abundance. Pyrite is also abundant in the epithermal veins, but contains significantly less Au than arsenopyrite. All other sulfides, sulfosalts and alloys occur only in trace amounts and are not considered to be of economic importance despite their partly high Au-content (Table 2).

Table 2. Au-contents of the investigated phases as determined by in-situ LA-ICPMS analyses.

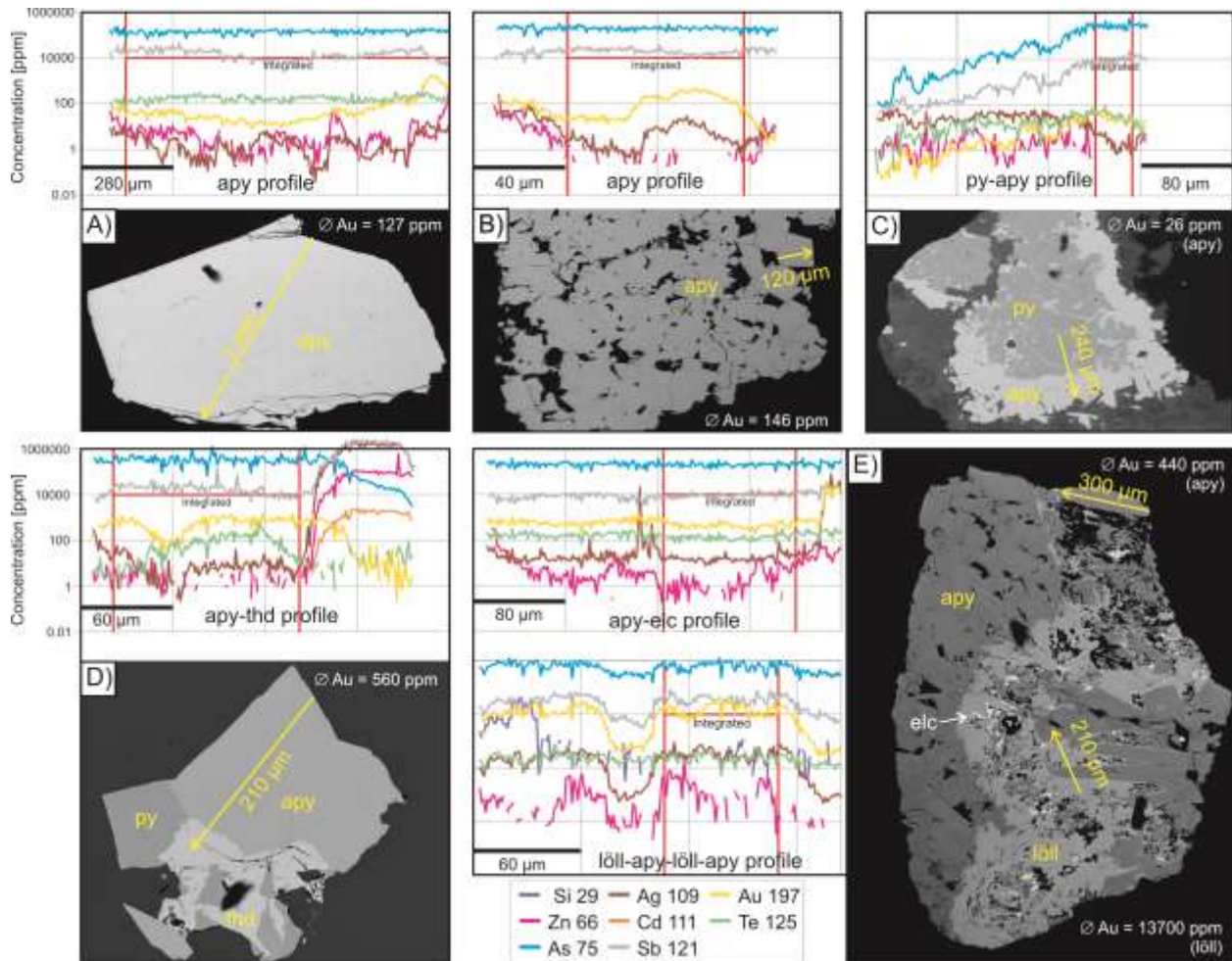| Phase	Average Au [ppm]	Number of analysis
arsenopyrite	131 (max. 560 ppm)	50
pyrite	3.43	82
chalcopyrite	0.16 (mostly b.d.l.*)	5 (3 with Au b.d.l.)
hessite	328	1
löllingite	9491	7
pyrrhotite	0.18 (mostly b.d.l.)	3 (2 with Au b.d.l.)
sphalerite	0.47	19
stibarsen	11.2	13
tetrahedrite	1.70	5

*b.d.l. = below detection limit

Fig. 22. Trace element profiles (TEPs) across various phases (apy = arsenopyrite; py = pyrite, thd = tetrahedrite; löll = löllingite, elc = electrum) and BSE images showing the location of the measured profiles (yellow arrows). The LA-ICPMS analyses may reveal sub-surface features/phases that are not visible on the BSE images due to a laser penetration depth of ~20-30 µm. The average Au-contents shown in the BSE images were determined from the 'integrated' intervals shown in the profiles. The element concentrations in thd shown in (D) are exaggerated, because the profile was calibrated based on Fe in apy and not thd. (A) and (B) TEPs of apy crystals showing zonations in the Au-distribution. (C) TEP across py and apy. The correlation between As-Sb and Au indicates that apy is the main host for Au. The contrary holds true with respect to Ag. (D) TEP across apy and thd showing an Au-zonation in the apy and a lower Au-content in thd as compares to apy. Cd correlates with Ag, Sb and Zn in thd. (E) TEP (300 µm) across apy and elc. The Ag-spike in the profile probably reflects an acanthite inclusion. TEP across löll-apy-löll-apy (210 µm) showing a positive correlation between Au, Ag, Sb and As. Löllingite is characterized by higher Au-contents than arsenopyrite.
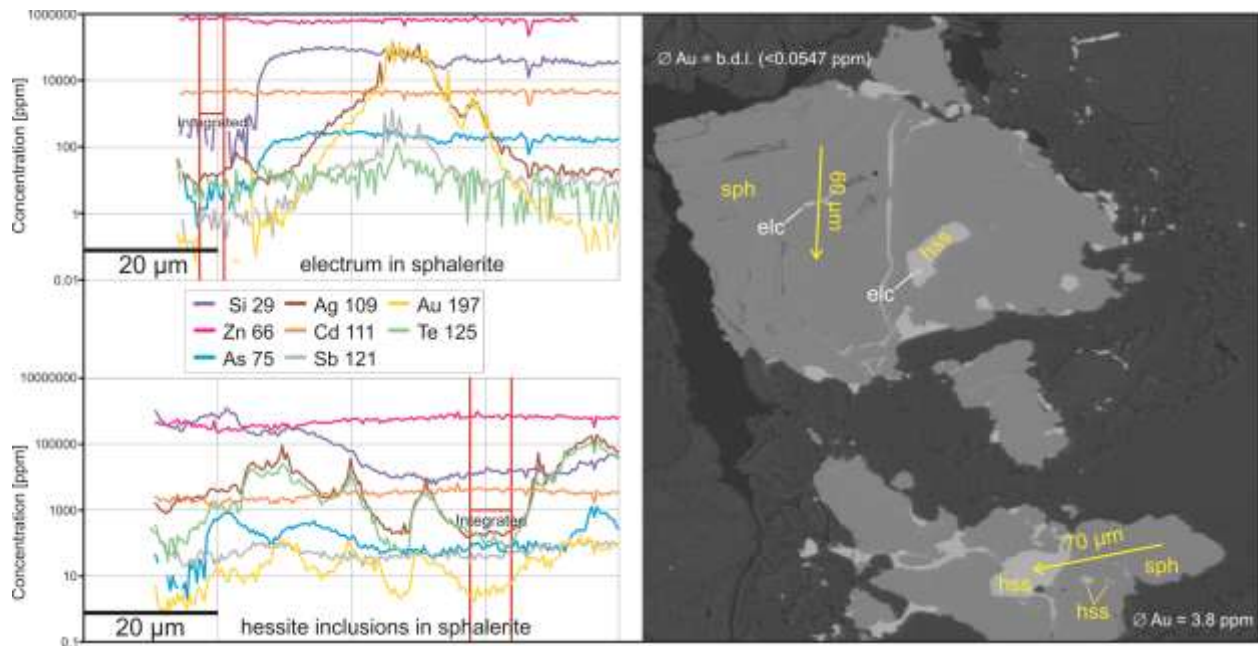
Fig. 23. Trace element profiles across sphalerite (sph) with inclusions of electrum (elc) and hessite (hss; Ag$_2$Te). The Au-content of pure sph is generally low (<0.5 ppm), however, Au-rich inclusions of elc and hess in sph are common. The correlation between Ag, Te and Au in the lower profile indicates that the Au is hosted in hessite. The high amount of Si indicates that the laser did penetrate the sph, elc and hss grains during ablation.

Fluid inclusion studies

The quartz textures discussed in section 'Quartz (qtz)' indicate that during ore formation silica precipitated as amorphous silica or chalcedony, which subsequently recrystallized to quartz (Figs. 17a-d). Due to the very fine grain size of the original precipitates they rarely contain fluid inclusions large enough to study (Bodnar et al., 1985). In addition, fluid inclusions in this type of recrystallized quartz do not record the P-T-x conditions of the ore forming hydrothermal fluid, but the fluid conditions during quartz recrystallization (cf. Moncada et al., 2012; Sillitoe and Hedenquist, 2003). In contrast, primary fluid inclusions in quartz, which directly grew from a hydrothermal fluid, such as zonal quartz (Fig. 17f; Dong et al., 1995), are interpreted to record fluid conditions during quartz growth. Fluid inclusions analyzed in this study consist of two types; (1) irregular to round shaped, up to 20 µm large fluid inclusions from growth zones in zonal quartz (Figs. 17d-f), and (2) irregular, up to 15 µm large fluid inclusions in plumose quartz of the ore forming stage (II) (Figs. 17a-b). If possible, i.e. for type (1) fluid inclusions, only growth zones in quartz where the fluid inclusion assemblages have consistent fluid-to-vapor ratios were selected for analyses (Fig. 24; cf. Bodnar et al., 1985).
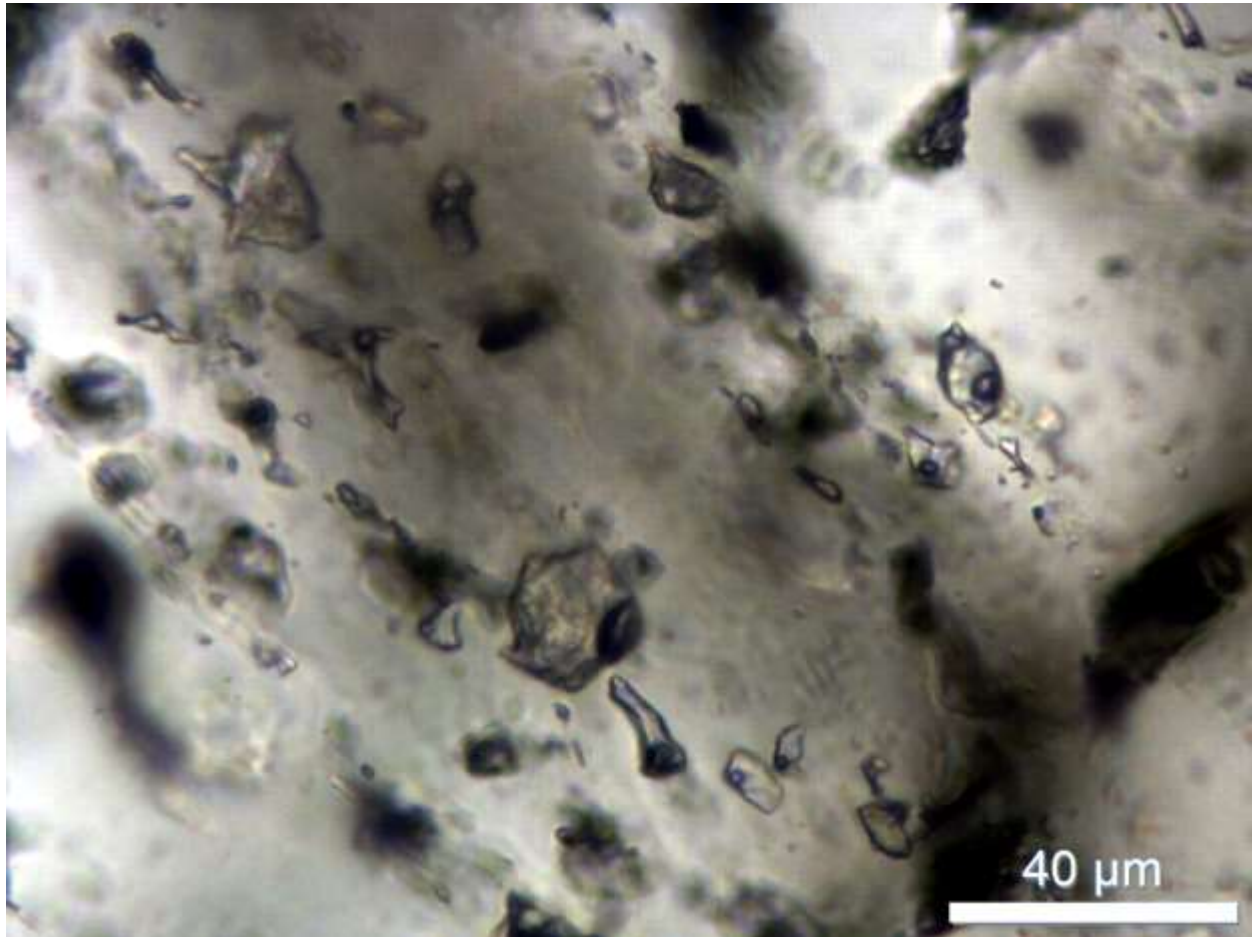
Fig. 24. Fluid inclusion assemblage of type (1) fluid inclusions in zonal quartz showing consistent liquid-to-vapor ratios. These fluid inclusions yielded T_h of 187 to 197 °C.

The ice melting temperatures (T_m) and homogenization temperatures (T_h) for type (1) fluid inclusions (n = 24) from a sample of the DD-Vein range from -0.4 to -0.3 °C, and 179 to 220 °C, respectively. In contrast, type (2) fluid inclusions (n = 27) from a sample of the E-Vein yielded T_m = -0.4 to -0.1, and T_h = 140 to 157 °C.

Based on the assumption that zonal quartz grows under slow changing or very mildly fluctuating fluid conditions (Fournier et al., 1985; in Dong et al., 1995) type (1) fluid inclusions indicate that the investigated quartz grew from a low-salinity fluid (wt% $NaCl_{eq}$ = 0.2 to 0.7) at temperatures of ~180 to 220 °C. In contrast, type (2) fluid inclusions indicate that amorphous silica of the ore-forming stage (II) recrystallized to quartz at T = 140-157 °C while in contact with a low-salinity fluid. These results are in general agreement with previous studies (Mihalynuk et al., 1999a), which yielded T_h of 195 and 171 °C, and T_m of -0.2 and 0.0 °C for fluid inclusions in quartz from the Engineer and Double Decker Vein, respectively. However, although type (1) fluid inclusions are contained in 'zonal' quartz, textural evidence suggests that this quartz may in fact represent plumose quartz that has experienced substantial recrystallization. These fluid inclusions would then be 'pseudoprimary' inclusions and do not record primary fluid conditions during deposition (Sander and Black, 1988). Therefore, fluid inclusions from both samples may record the conditions under

which quartz recrystallized. However, the obtained temperatures are consistent with those expected in the epithermal environment (Cooke and Simmons, 2000), and salinities close to zero suggest that meteoric water played a major role in the Engineer Mine epithermal system. In addition, zonal quartz also contains rare vapor-only fluid inclusions, suggesting that liquid-vapor phase separation occurred in the Engineer Mine epithermal system at one point.

Hydrogen, oxygen and carbon isotope studies

In order to further characterize the hydrothermal fluid(s) that formed the Engineer Vein, and to complement the fluid inclusion studies, H- and O-isotope analyses were conducted on V-mica intergrown with electrum (Figs. 6e and 8a), and the C- and O-isotopy of vein calcite from various mine levels was determined. The results are summarized in Figure 25.

The δ^{18}O and δD values of V-mica samples from the 5th mine level range from -3.7 to -5.6‰ (±0.1‰) and from -150 to -146‰ (±1‰), respectively, relative to VSMOW. Assuming equilibrium was attained during isotopic fractionation between V-mica and the hydrothermal fluid, and applying the homogenization temperatures obtained from fluid inclusion studies (T_{min} = 150 °C; T_{max} = 220 °C), the isotopic composition of the hydrothermal fluid can be calculated. The δ^{18}O$_{fluid}$ and δD$_{fluid}$ values were calculated using the fractionation expressions of Sheppard and Gilg (1996; illite-water) and Suzuoki and Epstein (1976; muscovite-water), respectively. The results indicate that at T = 220 °C the isotopic composition of the fluid coincides with the meteoric water line (Craig, 1961; Fig. 25a). In contrast, at lower temperatures, the δ^{18}O and δD isotopy of the fluid attains values that are not realized in nature (cf. Campell and Larson, 1998).

Carbon and oxygen isotope analyses were carried out on vein carbonate samples (n = 14) from various mine levels of the Engineer Vein, as well as different veins. Using short wave UV-light two optically different types of carbonate could be distinguished. Type (1) shows bright red fluorescence, whereas type (2) is violet in color (Figs. 25c and d, and 6b).

Both types can be associated with ore mineralization and can occur next to, or apart from each other. In spite of the optical differences and the lateral (~400 m) and vertical extent (~150 m) covered by the samples, the obtained δ^{13}C (PDB) and δ^{18}O (VSMOW) values for vein calcite fall within limited ranges. The measured δ^{13}C and δ^{18}O values range from -5.0 to -3.6‰, and -3.9 to -7.1‰, respectively. The internal precision (1SE) is <0.5‰ for δ^{13}C$_{VPDP}$ and <0.6‰ for δ^{18}O$_{VSMOW}$ (Barker et al., 2011). The δ^{18}O and δ^{13}C isotopic composition of the hydrothermal fluid in equilibrium with vein calcite was calculated using the fractionation expressions of O'Neil et al. (1969; calcite-water) and Deines et al. (1974; CO$_2$-calcite). Calculated δ^{13}C$_{fluid}$ and δ^{18}O$_{fluid}$ values range from -11.9 to -15.1‰, and -6.3 to -4.9‰, respectively (Fig. 25b).

In contrast, sedimentary carbonate layers within the argillite host rock and carbonate related to the early carbonate-pyrrhotite alteration yield substantially different δ^{13}C and δ^{18}O values (Fig. 25b). Coarse grained dark sedimentary calcite, showing no luminescence, has δ^{13}C and δ^{18}O values of -7.4‰ and -18.0‰, respectively. Furthermore, fine to coarse grained dark-grey to white granular

carbonate with red luminescence and related to the early alteration event has $\delta^{13}C$ and $\delta^{18}O$ values of -1.9‰ and 14.2‰, respectively.

Based on these results, we conclude that the main ore assemblage, represented by V-mica and electrum, was formed at ~220 °C from a fluid with the isotopic composition (i.e. $\delta^{18}O$ and δD) of meteoric water. This interpretation is in agreement with the salinities obtained from fluid inclusion studies and the calculated $\delta^{18}O$ values of a fluid in equilibrium with vein calcite (Fig. 24a). Furthermore, $\delta^{18}O$ and $\delta^{13}C$ values of vein calcite in combination with values of sedimentary calcite and calcite related to the early alteration event suggest that the isotopic composition of the hydrothermal fluid was attained by equilibration with those two sources of carbonate. Figure 25b further indicates that the influence of sedimentary carbonate on the isotopic composition of the fluid dominated over that from calcite related to the early alteration.
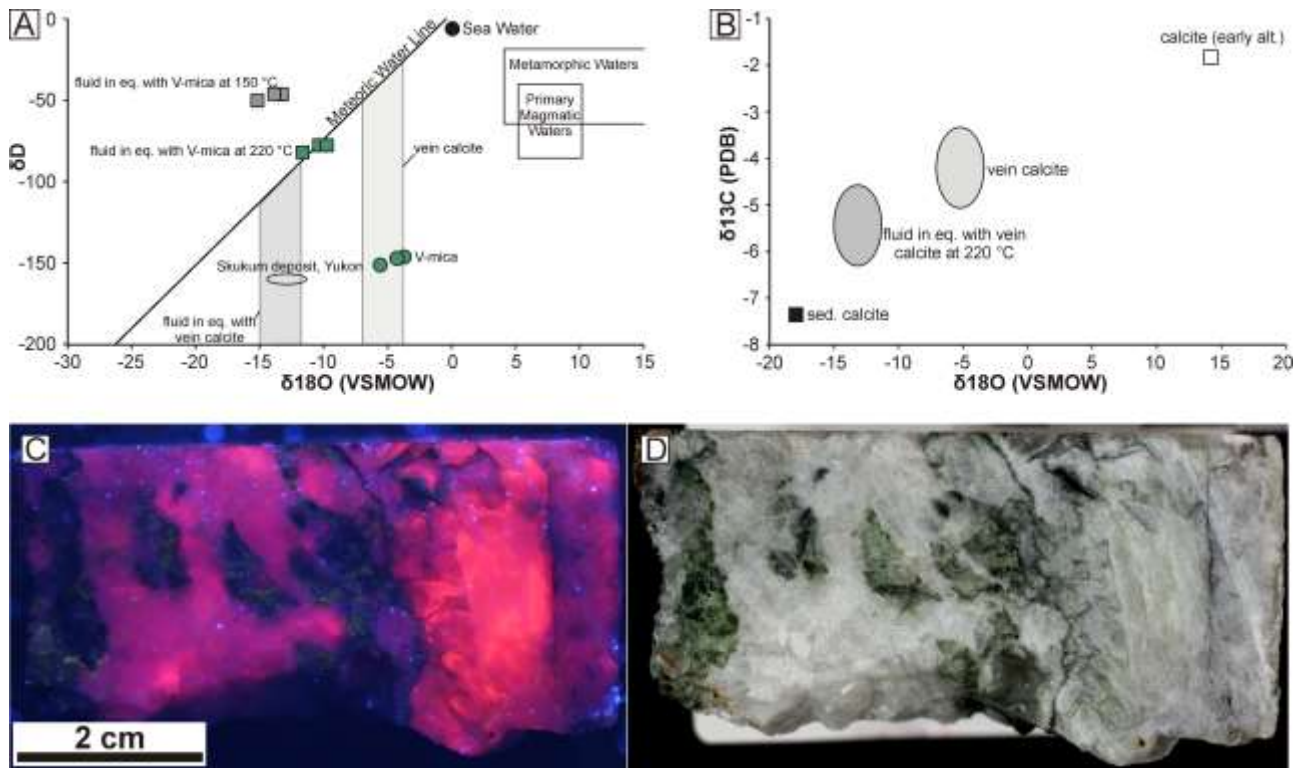

Fig. 25. Diagrams depicting the oxygen and hydrogen isotopic compositions of V-mica of the ore forming stage (A), and the oxygen and carbon isotopic compositions of calcite (B). (A) The isotopic composition of fluid in equilibrium with V-mica (white circles) calculated for 220 °C (white boxes) coincides with the meteoric water line. In contrast, using lower temperatures (150 °C, grey boxes) yields isotopic compositions not realized in nature. (B) The two different types of vein calcite (see text) show similar isotopic compositions, but are distinct from sedimentary calcite and calcite related to the early alteration event. The isotopic composition of the fluid (blue boxes) in equilibrium with vein calcite is interpreted to result from homogenization with these two types of calcite. Furthermore, the isotopic composition of this fluid is in good agreement with the fluid composition calculated from the isotopic composition of V-mica of the ore forming stage shown in (A). (C and D) Two types of vein calcite (bright red vs. violet color; see also Figure 6b) shown under ultraviolet (C) and normal light (D). Both calcite types have similar $\delta^{18}O$ (VSMOW) and $\delta^{13}C$ (PDB) isotopic compositions.

Geochemistry of the Sloko-Skukum Group volcanics and the Source of Vanadium

The Sloko Group volcanics are remnants of a continental arc and consist mainly of rhyolitic to andesitic flows, breccia, tuff and ignimbrite and derived epiclastic rocks (Mihalynuk et al., 1999a). These volcanic rocks are considered to be correlative to the high-K calc-alkaline to shoshonitic Skukum Group volcanics of the Yukon Territory (Morris and Creaser, 2003; Love, 1997). These rocks are jointly referred to as the Sloko-Skukum Group (SSG; Miskovic and Francis, 2006). The SSG comprises the Sloko Lake (Resnick 2003) and Sifton Range Volcanic Complexes (Miskovic and Francis, 2006) and the Bennet Lake and Mount Skukum Volcanic Complexes (Morris and Creaser, 2003) (Figs. 26a to d), amongst others. In the TAS (total alkali-silica) classification diagram the SSG volcanics straddle the dividing line between alkaline and subalkaline rocks (Fig. 26a). However, the samples investigated during this study are marked by comparatively high alkali-contents which are interpreted to result from potassic alteration, causing an increase in the total alkali content and thus a shift towards the alkaline series. In contrast, in the Zr/TiO_2 vs. Nb/Y diagram the vast majority of the SSG volcanics are unambiguously classified as subalkaline (Fig. 26b). The SSG volcanics are thus characterized by alkaline-contents approaching those of alkaline rocks, whereas their immobile trace element ratios such as Nb/Y are characteristic for subalkaline rocks. In addition, the SSG volcanics are neither distinctively tholeiitic, nor calc-alkaline in nature (Fig. 26c) (Resnick, 2003). Contrarily, Miskovic and Francis (2006) argue that rocks of the Sifton Range volcanic complex display a calc-alkaline differentiation trend in terms of continuously decreasing TiO_2 with increasing FeO*/MgO, whereas Morris and Creaser (2003) argue that rocks of the Bennet Lake and Mount Skukum volcanic complexes follow a tholeiitic trend. These bivalent geochemical characteristics of the SSG volcanics are interpreted to result from subduction-induced partial melting of the crust and the coeval presence of primitive magmas, which contaminated the crustal melts during eruption (Morris and Creaser, 2003). The SSG volcanics, furthermore, display a magmatic evolution from basalt to rhyolite (Figs. 26a and b). This evolution is corroborated by a systematic change in the V-content (Fig. 26d), as discussed below. The chemical compositions of the Sloko Group volcanics investigated during this study are given in Appendix C1.
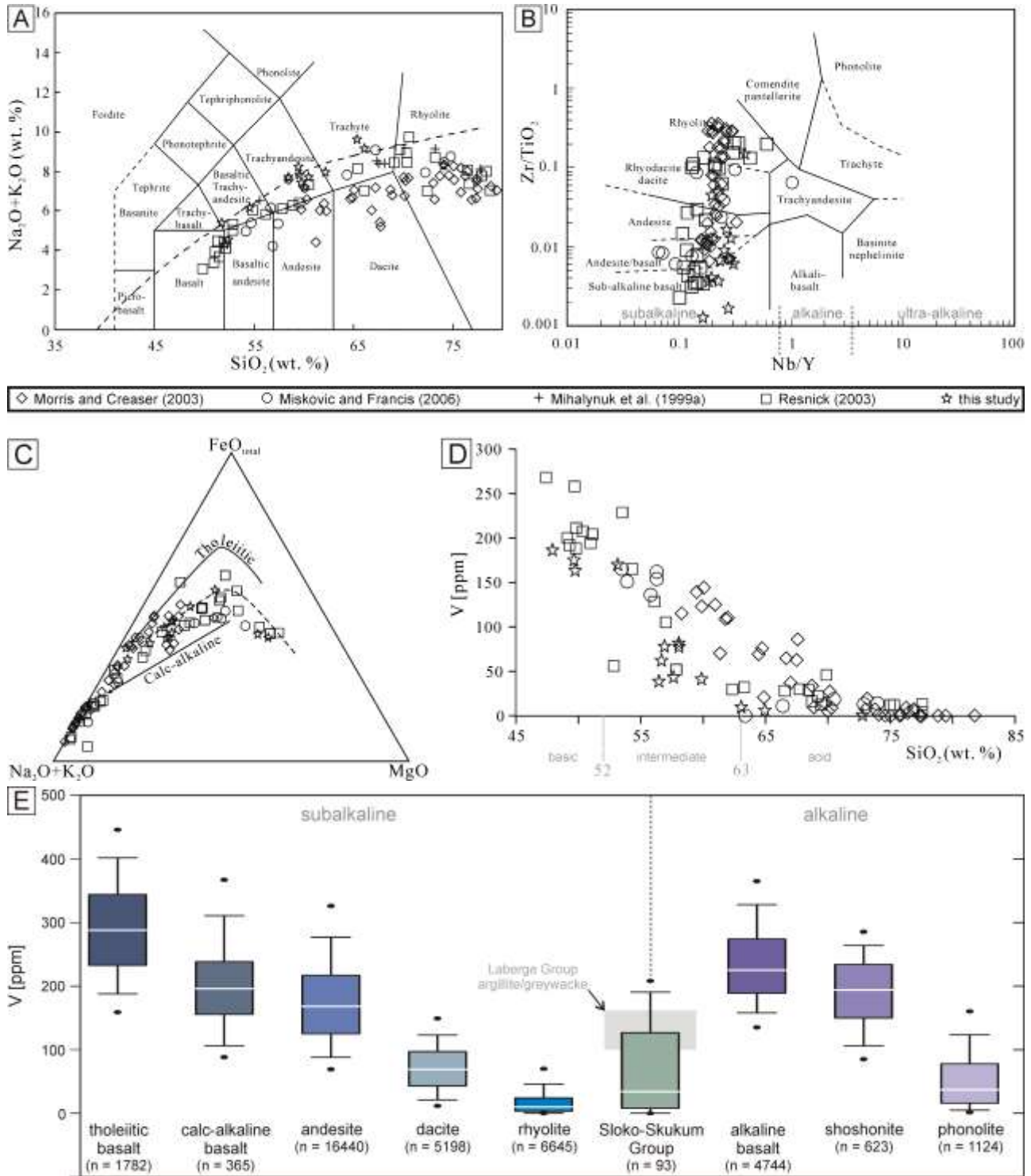
Fig. 26. (A), (B) and (C) Geochemical classification of the Sloko-Skukum Group (SSG) volcanics using the TAS (total alkali-silica) diagram (modified after Le Bas et al., 1986), the Zr/TiO_2 vs. Nb/Y diagram (modified after Winchester and Floyd, 1977 and Pearce, 1996) and the AFM diagram (after Irvine and Baragar, 1971). Data plotted with CGDK (Qiu et al., 2013). (A) The SSG volcanics are alkali-rich but mostly subalkaline in character. However, some samples straddle the alkaline-subalkaline dividing line or plot in the alkaline part of the diagram. (B) Based on immobile element ratios the SSG volcanics are classified as subalkaline. (C) The SSG volcanics are neither distinctively tholeiitic, nor calc-alkaline in nature. (D) Vanadium vs. SiO_2 plot of the SSG volcanic, which show a systematic decrease in V-content with increasing silica-content for SiO_2 <75 wt%. (E) Comparison of the V-contents of various subalkaline and

alkaline volcanics (data from GEOROC, 2015; Appendix D) and Laberge Group argillite and greywacke (n = 2). Neither of the two magmatic rock groups is enriched over the other with respect to vanadium. However, the V-content decreases systematically the more evolved a magmatic series gets, *e.g.,* from andesite to dacite to rhyolite. The alkaline rocks correspond to the general volcanic rock types associated with the Porgera (alkali basalt to mugearite; Ronacher et al., 2002), Emperor (shoshonite; Scherbarth and Spry, 2006) and Cripple Creek (phonolite; Kelley et al., 1998) deposits.

The fact that epithermal deposits related to alkaline magmatism are characterized by the occurrence of roscoelite (V-mica), tellurides and fluorite (Jensen and Barton, 2000) poses the question if alkaline rocks are generally richer in vanadium than subalkaline rocks and thus favor the crystallization of V-bearing phases. A comparison of the V-contents of various subalkaline and alkaline volcanics shows that neither of the two groups is enriched over the other with respect to vanadium (Fig. 26e). However, Figure 26e illustrates that the V-content of volcanic rocks systematically decreases during their magmatic evolution, *e.g.,* from tholeiitic or calc-alkaline basalt to andesite to dacite to rhyolite. This observation also holds true for the Sloko-Skukum Group volcanics, which show a systematic decrease in V-content with increasing SiO_2-content, especially for SiO_2 <75 wt% (Fig. 26d). Similarly, Barton and Jenson (2000) emphasize the correlation between vanadium enrichment and the proportion of mafic and felsic rocks in alkaline epithermal deposits. Thus, the formation of V-bearing phases is favored in deposits related to less evolved magmas. However, the fact that neither alkaline nor subalkaline volcanics are per se enriched in vanadium, as well as the presence of V-bearing phases in orogenic gold deposits such as the Hemlo deposit, Ontario, indicates that other factors than the composition of the associated magmatic rocks may determine if V-bearing phases precipitate at a given (epithermal) deposit. A possible factor is the composition of the host rock and its interaction with the ore-forming fluid. This hypothesis is supported by the fact that no V-bearing minerals have been reported from the epithermal Mount Skukum Au-deposit, Yukon, which is also related to Eocene Sloko-Skukum Group volcanism (Mihalynuk et al., 1999a). In contrast to the Engineer Mine, which is hosted by Laberge Group argillite and greywacke with V-contents of ~105-170 ppm, the Mount Skukum deposit is hosted by SSG volcanics with an average V-content of ~30 ppm (Figs. 26d and e).

Discussion

Ore assemblage and mechanism of ore precipitation
The paragenetic sequence for the Engineer and Double Decker Veins indicates that the principal ore assemblage precipitated during a single hydrothermal event (cf. Sibson, 1987). During this event electrum, arsenopyrite, pyrite, ±chalcopyrite, ±sphalerite, ±löllingite, ±tetrahedrite-group phases, ±allargentum, ±acanthite, ±hessite, ±dyscrasite, ±stibarsen, ±galena, as well as unidentified Ag-bearing phases were deposited in conjunction with amorphous silicia or chalcedony (now recrystallized to quartz), platy and rhombic calcite, K-feldspar, and (V-)illite. Moreover, textural evidence suggests that besides quartz, calcite and V-illite were also in part originally precipitated in amorphous form.

Vein and mineral textures of the ore-forming stage are indicative of supersaturation (Adamson and Gast, 1997) of the hydrothermal fluid with respect to the aforementioned mineral species. Based on

mineralogical and textural evidence, this supersaturation was due to rapidly changing P-T-x fluid conditions in response to boiling (Henley, 1993; Hedenquist et al., 2000), as manifested by the crystallization of platy calcite (Simmons and Christenson, 1994), K-feldspar (Browne, 1978; Simmons and Hedenquist, 2000), and vapor-only fluid inclusions in quartz. Textural evidence further indicates that during boiling platy calcite, as well as rhombic calcite precipitated and that the availability of space determines to a large degree which crystal habit will develop. Boiling is in fact the favored mechanism for the precipitation of gold in low-sulfidation epithermal systems due to an increase in pH and a decrease in HS^- in the residual liquid, resulting from the loss of CO_2 and H_2S to the vapor phase (Browne and Ellis, 1970; Heinrich, 2007; Williams-Jones et al., 2009). This liquid-vapor phase separation can also lead to the co-precipitation of base-metal sulfides like pyrite or sphalerite (Heinrich, 2007), as observed during this study. Another effect of boiling is the loss of heat to the vapor phase and thereby cooling of the liquid (Drummond and Ohmoto, 1985). Notably, most of the gold transported in a hydrothermal fluid may be precipitated over a small temperature interval when boiling occurs (Seward, 1993; Simmons and Hedenquist, 2000).

The effect of boiling and the related supersaturation of the fluid with respect to certain compounds is also expressed in the formation of colloform-crustiform vein textures (Fournier, 1985; Dong et al., 1995; Hedenquist, 2000), such as botryoidal stibarsen (Rahmdohr, 1980) or amorphous silica, as well as acicular, skeletal, dendritic, spherical and vermicular crystal habits, as observed in the investigated samples (Figs. 9a-e, 11a, 20a-d). The respective crystal morphologies are dependent on the degree of disequilibrium, due to, *e.g.,* undercooling (Lofgren, 1974), and thus the degree of supersaturation of the melt (Fig. 27) (Drever et al., 1972) or fluid, as well as the correspondent crystal growth velocity (Tiller, 1960; in Lofgren, 1974). The crystal growth rate is in turn related to the diffusion coefficients of the components necessary for growth and hence the viscosity of the melt (Lofgren, 1974) or fluid. For example, Lofgren (1974) used melted plagioclase gels to investigate the effect of undercooling to the crystal morphology and found that it is strongly "*dependent on the degree of supercooling ΔT, changing from tabular crystals at small ΔT to skeletal crystals, dendrites, and spherulites with increasing ΔT*". The particular crystal shape of a mineral will further depend on its crystal system (Lofgren, 1974). Similar conclusions hold true for the non-equilibrium solidification of undercooled alloys (cf. Boettinger and Coriell, 1986). In case of the Engineer Mine hydrothermal system, evidence for undercooling is provided by microtextures in stibarsen (Fig. 15), which resemble those formed during undercooling-solidification experiments of alloys (Han and Wei, 2002). These similarities are intriguing and conform well to the constraints imposed by other vein and mineral textures, but without further investigation it cannot be ruled out that they represent secondary solid-state exsolution textures. Furthermore, alternating layers of arsenopyrite and löllingite (Figs. 9e and f), the latter of which are associated with electrum, attest fluctuations in the S-fugacity of the hydrothermal fluid during ore formation and that the precipitation of electrum was favored by low S-fugacities. This is in accordance with the notion that the loss of H_2S to the vapor phase during boiling causes gold to precipitate (Williams-Jones et al., 2009).
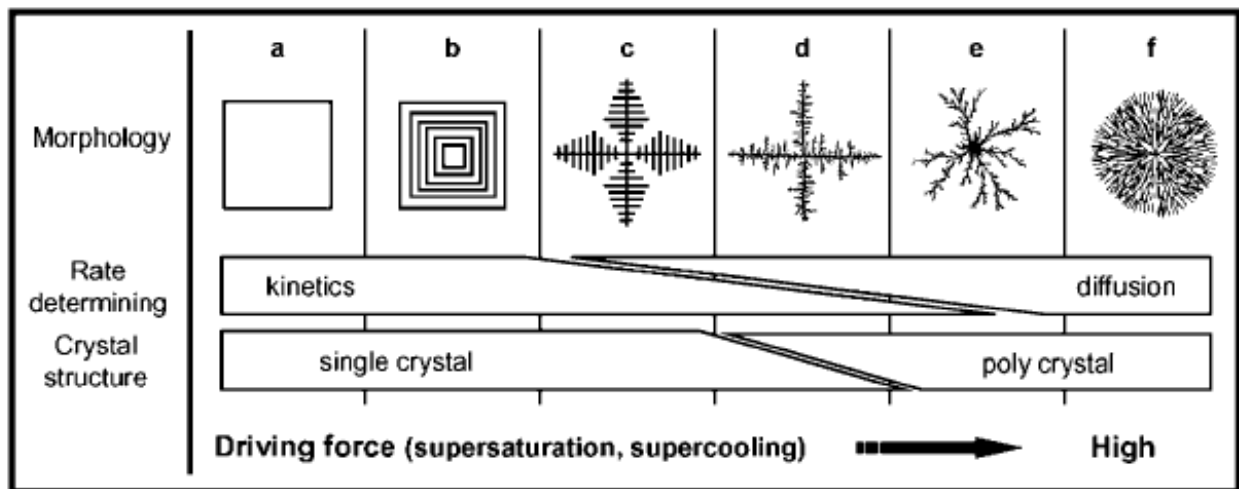
Fig. 27. Schematic model of morphological evolution with an increase in the driving force: (a) polyhedral form produced in the kinetic-controlled system near equilibrium, (b) skeletal morphology by the Berg effect, (c) single-crystalline ordered dendrite with crystallographic symmetry, (d) partially disordered dendrite having a single-crystalline ordered trunk and disordered polycrystalline side branches, € disordered polycrystalline dendrite as shown in diffusion-limited aggregation, and (f) dense branching morphology (from Oaki and Imai, 2003).

Considering the above aspects it is apparent that boiling affected various parameters of the Engineer Mine hydrothermal fluid, including temperature, pH and HS⁻, and thereby controlled its degree of supersaturation with respect to certain mineral-forming compounds. This supersaturation resulted in mineral deposition and the formation of vein and mineral textures, specific for each mineral and depending on the local physicochemical conditions of the fluid. These local variations imply that it is possible that '*at any time different* (mineral) *assemblages* (and textures) *were formed in different parts of the mine*' (Ahmad et al., 1987).

Mineral textures and static recrystallization
An important aspect of disequilibrium mineral textures, *e.g.,* caused by rapid precipitation due to supersaturation, is that they represent metastable states, and that a rock, quartz-carbonate vein in this case, tends to reduce its internal free energy by recrystallization processes, such as static recrystallization (Passchier and Trouw, 2005; and references therein). This process describes the transformation of a (fine grained) polycrystalline material with irregular grain boundaries into a fabric with larger, polygonal grains with straight grain boundaries. Furthermore, static recrystallization is promoted by elevated temperatures and the presence of water along grain boundaries (Passchier and Trouw, 2005). In geothermal systems the recrystallization of noncrystalline opal-A containing 4-10 wt% H_2O to microcrystalline quartz containing <0.2 wt% H_2O liberates abundant water (Herdianita et al., 2000). The study by Herdianita et al. (2000) also showed that this recrystallization can occur in geological short time spans and is pressure and temperature dependent (Bettermann and Liebau, 1975; Oehler, 1976). Moreover, the highly variable grain size of, *e.g.,* quartz in the investigated samples may in parts also be attributed to static recrystallization, because the resultant grain size of this process is dependent on the thickness of the layer of the original material (Passchier and Trouw, 2005). With respect to this study this means that the thicker the original layer or concretion of the amorphous substance (*e.g.,* silicic or

micaceous), the coarser the recrystallized crystals will be. Considering the nature of the epithermal veins at the Engineer Mine, i.e. elevated temperatures, abundant water, and Eocene age, substantial recrystallization of, *e.g.,* amorphous silica to quartz is to be expected and in accordance with textural evidence.

This recognition is also crucial for fluid inclusion studies, because textural observations suggest that at least some of the 'zonal' textured quartz, which is generally regarded as being a primary texture (Dong et al., 1995), is in fact substantially recrystallized plumose quartz (Sander and Black, 1988). It also poses the question if the water/fluid liberated during recrystallization could have been trapped in-situ as fluid inclusions in the recrystallizing quartz.

In addition, the mutual development of euhedral crystal habits of adjacent quartz and calcite (Fig. 18g) is interpreted to indicate their simultaneous precipitation in presumably amorphous form, as indicated by plumose quartz. Under the premise that the mineral textures shown in Figure 18h (cf. 18i) are due to the recrystallization of amorphous carbonate to calcite and the surrounding silica to plumose quartz, they further imply that the force of crystallization is greater for quartz than for calcite. Therefore quartz is more likely to develop an eu- to subhedral crystal habit, opposed to anhedral calcite. In rare instances, however, the force of crystallization, and thus the ability to develop euhedral crystal shapes, seems to be equal for quartz and calcite (Fig. 18g). This complicates textural interpretations considerably, because it obscures the relationships needed to deduce the chronological order of crystallization, or rather precipitation. As an example, if amorphous carbonate and silica precipitate together, and only quartz develops a euhedral habit in contact with calcite, the resulting texture will be similar to secondary calcite filling a quartz vug.

Hydrothermal fluid conditions during ore precipitation

Stable isotope analyses, in combination with fluid inclusion studies constrain that the ore-forming fluid had a temperature of ~220 °C and an isotopic composition ($\delta^{18}O$ and δD) similar to meteoric water. The later conclusion was also reached by McDonald (1987) for the low-sulfidation epithermal Mt. Skukum Au-Ag deposit, which is of similar age as, and located about 100 km northwest of the Engineer Mine (Love, 1997). Our inferred fluid temperature of ~220 °C is also in good agreement with the formation temperature of sericite/illite of ~200 °C (Meunier and Velde, 2004) and fits the main ore assemblage of V-illite and electrum in the Engineer and Double Decker Veins. Furthermore, carbon and oxygen isotope analyses of vein and sedimentary carbonates indicate that the hydrothermal fluid attained its $\delta^{18}O$ and $\delta^{13}C$ composition due to interaction with the host rocks. These findings are consistent with the characteristics of epithermal quartz ± calcite ± adularia ± illite deposits (Tosdal et al., 2009) also referred to as epithermal low-sulfidation deposits (see discussion in Sillitoe and Hedenquist, 2003). Furthermore, the low salinities (<0.7 wt% NaCl equiv) obtained from fluid inclusion studies correspond to those of low-sulfidation deposits related to tholeiitic and calc-alkaline magmatism (<2 wt% NaCl equiv), but contrast to those related to alkaline magmatism (3 to 9.6 wt% NaCl equiv; Richards, 1995; in Sillitoe and Hedenquist, 2003). The presence of tellurides, albeit in accessory amounts, however, suggests a deposit type related to alkaline magmatism. The presence of roscoelite, which is also regarded as indicative for epithermal

deposits related to alkaline magmatism, could not be confirmed during this study. Chemical analyses instead indicate that the dark-green mica associated with electrum is V-bearing illite that formed as a primary gangue phase. These observations indicate that the Engineer Mine shares characteristics of epithermal deposits related to tholeiitic to calc-alkaline, as well as alkaline magmatism (Sillitoe and Hedenquist, 2003; Jensen and Barton, 2000).

Constraints on the extent of the ore zone

The occurrence of platy (bladed) calcite, in conjunction with K-feldspar, is regarded as indicative of boiling of the hydrothermal fluid. Since boiling is regarded as the dominant process for ore precipitation in the Engineer and Double Decker Veins, constraining the depth limits of platy calcite should shed some light on the extent of the ore zone. For example, in the Broadlands-Ohaaki and Kawerau geothermal systems, New Zealand, platy calcite is restricted to within 300 m above the zone where fluids begin to boil (Tulloch, 1982; in Simmons and Christenson, 1994). In the investigated samples platy calcite was observed between the 8 level (592 m el.) and 5 level (684 m el.). This, however, does not constraint the lower limits of the occurrence of platy calcite due to a lack of samples from deeper mine levels. This suggests that the lower limit of the ore zone, i.e. the boiling horizon, has not been reached yet, and that the lower, less developed mine levels are likely to contain high-grade ore. This conclusion is supported by visible gold observed by the author on the 7th mine level (627 m el.), and results of geochemical assays from that level (BCGold Corp., 2012). In addition, BCGold drill hole BCGE10-01 intersected banded and brecciated, vuggy quartz veins containing electrum / V-illite, 21 m below 8 Level (~570 m el.) on the DD Vein which averaged 22.32 g/t Au over 0.96 m confirming historic samples from workings on the 8th mine level.

Age and structural relationships of the Engineer Mine hydrothermal system

According to available chronological data, the formation of the precious metal-bearing veins at the Engineer Mine at ~50 Ma (K/Ar-Ar on vein roscoelite; Devine, 2012; unpublished data) postdates local Sloko Group volcanism by ~4 Ma (54.1 ± 0.14 Ma; U-Pb on zircon from rhyolite on top of Engineer Mountain; Gabites, in Mihalynuk et al., 1999a). Field evidence, however, suggests that the intrusion of the youngest dykes related to Sloko Group volcanism overlaps with the earliest hydrothermal activity (Devine, 2008). These observations, though contradicting, suggest that the formation of the epithermal veins occurred during the waning stages of Sloko Group volcanism. A similar chronological discrepancy has been reported from the Skukum mine, which is also related to Eocene Sloko Group volcanism. Here adularia-sericite alteration, which envelopes epithermal Au-veins, is apparently 2 Ma younger than the enclosing volcanics (Mihlaynuk et al., 1999; and references therein). The reasons for this discrepancy are not yet fully understood, but with respect to the Engineer Mine, recrystallization of 'roscoelite' (i.e. V-illite) may have disturbed the isotopic equilibrium (Meunier and Velde, 2004).

Eocene fault reactivation of the Llewellyn fault and associated splays, such as Shear-A, concomitant with Sloko Group volcanism, is considered a controlling factor for the emplacement and orientation of the Engineer and Double Decker Veins (Devine, 2008). Taking this into account,

boiling of the hydrothermal system was most likely triggered by fault movement along Shear-A and fracturing of the host argillite. These fractures temporarily created pathways for the hydrothermal fluid (Sibson, 1987) and sharp gradients in pressure and density of crustal fluids, which lead to boiling of the fluid. The textural evidence presented in this study suggests that it was the initial fracturing that caused boiling and precipitation of the ore phases. We emphasize, though, that some of these pathways (*e.g.,* E-Vein) may have been active for an extended time period, and that subsequent fluid flow partly brecciated and overprinted earlier vein stages.

A possible scenario why only one ore forming event is recorded in the Engineer and Double Decker veins is that circulating hydrothermal fluids, which may already have been magmatically enriched in elements such as Au, Ag, As and Sb, scavenged those elements also from the country rocks over an extended time period. Subsequent fault activity caused brittle fracturing of the host rocks and boiling of the fluid leading to ore precipitation. It is plausible that this scenario could not be repeated because (1) the host rocks had already been extensively leached of precious metals, and subsequent fluids could therefore not reach a similar level of enrichment, or (2) subsequent fault activity was less intense and did not cause rapid changes in P-T-x of the fluid, thereby preventing ore precipitation.

Deposit model for the Engineer Mine

Based on vein textures, mineralogy and the results of fluid inclusions studies the Engineer Mine can be classified as an epithermal low-sulfidation deposit. Furthermore, the presence of only trace amounts of tellurides, as well as the low salinities of the ore-forming fluid (<0.7 wt% NaCl equiv) are characteristic for epithermal low-sulfidation deposits related to subalkaline magmatism (Sillitoe and Hedenquist, 2003). In contrast, the absence of selenides and the presence of V-mica are characteristic for epithermal deposits related to alkaline magmatism. Thus, the Engineer Mine shares characteristics of the subalkaline and alkaline epithermal deposit types (Table 4). This is attributed to the fact that the Sloko-Skukum Group volcanics are borderline subalkaline to alkaline and neither display a distinctively calc-alkaline, nor tholeiitic differentiation trend (Figs. 26a to c).

Table 4. Principal field-oriented characteristics of low-sulfidation epithermal deposit types (modified after Sillitoe and Hedenquist, 2003).

	Subalkaline magma	Alkaline magma	Subalkaline/alkaline magma
Type example	Midas, Nevada	Emperor, Fiji	Engineer Mine
Genetically related volcanic rocks	Basalt to rhyolite	Alkali basalt to trachyte	Basalt to rhyolite
Key proximal alteration minerals	Illite/smectite-adularia	Roscoelite-illite-adularia	Illite±kaolinite-carbonate[1]
Silica gangue	Vein-filling crustiform and colloform chalcedony and quartz; carbonate replacement texture	Vein-filling crustiform and colloform chalcedony and quartz; quartz deficiency common in early stages	Vein-filling crustiform and colloform chalcedony and quartz; carbonate replacement texture
Carbonate gangue	Present but typically minor and late	Abundant but not manganiferous	Abundant
Other gangue	Barite uncommon; fluorite present locally	Barite, celestite, and/or fluorite common locally	V-mica and adularia; fluorite present locally[2]

	Subalkaline magma	Alkaline magma	Subalkaline/alkaline magma
Sulfide abundance	Typically <1-2 vol % (but up to 20 vol % where hosted by basalt)	2-10 vol %	<1-5 vol %
Key sulfide species	Minor to very minor arsenopyrite ± pyrrhotite; minor sphalerite, galena, tetrahedrite-tennantite, chalcopyrite		Minor to very minor pyrite, arsenopyrite ± pyrrhotite; Very minor chalcopyrite, sphalerite, tetrahedrite-group phases
Main metals	Au ± Ag	Au ± Ag	Au ± Ag
Minor metals	Zn, Pb, Cu, Mo, As, Sb, Hg		Cr, Zn, As, Sb, Cu, Ni[3]
Te and Se species	Selenides common, tellurides present locally	Tellurides abundant; selenides uncommon	Tellurides present locally; selenides absent

[1]Fonseca (2008); [2]Mauthner et al. (1996); [3]in decreasing abundance (from BCGold Corp.'s 2010 drill assays)

Concluding remarks

The intimate association of gold and V-mica indicates that they are either transported together as Au-V-?-complexes in the hydrothermal fluid, or that they precipitate under similar P-T-x conditions. The exact mechanisms and reasons for their close association warrant further investigation, but are beyond the scope of this study.

Acknowledgements

References

Adams, S.F., 1920. A microscopic study of vein quartz. Economic Geology 15, 623–664.

Adamson, A.W., Gast, A.P., 1997. Physical Chemistry of Surfaces (Sixth Edition). John Wiley & Sons, Inc., pp. 784.

Ahmad, M., Solomon, M., Walshe, J.L., 1987. Mineralogical and geochemical studies of the Emperor gold telluride deposit, Fiji. Economic Geology 82, 345–370.

Aspinall, C., 2007. Report on the 2007 Season Surface and Underground Rock Sampling Program with Paragenesis Field Interpretations made on selected Vein Systems and Drill Core at Engineer Mine, Tagish Lake, Atlin Mining Division, British Columbia, Canada. Internal report prepared for BCGold. Corp., pp.108.

Barker, S.L.L., Dipple, G.M., Dong, F., Baer, D.S., 2011. Use of Laser Spectroscopy to Measure the 13C/12C and 18O/16O Compositions of Carbonate Minerals. Anal. Chem. 83, 2220–2226.

BCGold Corp., 2015. Corporate Presentation dated 08-Jan-2015, available at: http://www.bcgoldcorp.com/index.php?id=89&headerbar=6#pagetop.

BCGold Corp., 2012. News release dated 15-Nov-2011, available at: http://www.bcgoldcorp.com/index.php?id=127&news=164#pagetop

Bettermann, P., Liebau, F., 1975. The transformation of amorphous silica to crystalline silica under hydrothermal conditions. Contr. Mineral. and Petrol. 53, 25–36.

Bodnar, R.J., Reynolds, T.J., Kuehn, C.A., 1985. Fluid-inclusion Systematics in Epithermal Systems. Berger, B.R. and Bethke, P.M. (eds.), Reviews in Economic Geology 2, 73-96.

Boettinger, W.J., Corriell, S.R., 1986. Microstructure Formation in Rapidly Solidified Alloys. In Sahm, P.R., Jones, H., Adam, C.M. (Eds.). Science and Technology of the Undercooled Melt. Springer Netherlands, Dordrecht, 81-109.

Browne, P.R.L., 1978. Hydrothermal Alteration in Active Geothermal Fields. Annual Review of Earth and Planetary Sciences 6, 229–248.

Browne, P.R.L., Ellis, A.J., 1970. The Ohaki-Broadlands hydrothermal area, New Zealand; mineralogy and related geochemistry. Am J Sci 269, 97–131.

Campell, A.R., Larson, P.B., 1998. Introduction to Stable Isotope Applications in Hydrothermal Systems. Reviews in Economic Geology 10, 173-194.

Coates, B., 2012. Internal company report prepared for BCGold Corp., pp. 1.

Cooke, D.R., Simmons, S.F., 2000. Characteristics and Genesis of Epithermal Gold Deposits. SEG Reviews 13, 221–244.

Craig, H., 1961. Isotopic Variations in Meteoric Waters. Science, New Series 133, 1702–1703.

Deditius, A.P., Utsunomiya, S., Renock, D., Ewing, R.C., Ramana, C.V., Becker, U., Kesler, S.E., 2008. A proposed new type of arsenian pyrite: Composition, nanostructure and geological significance. Geochimica et Cosmochimica Acta 72, 2919–2933.

Deines, P., Langmuir, D., Harmon, R.S., 1974. Stable carbon isotope ratios and the existence of a gas phase in the evolution of carbonate ground waters. Geochimica et Cosmochimica Acta 38, 1147–1164.

Devine, F., 2008. Geological Report on the Engineer Property, British Columbia. Internal report prepared for BCGold Corp., pp. 110.

Devine, F., 2012. Summary of the preliminary SEM survey on a roscoelite-gold sample from the Engineer vein. Internal report for BCGold Corp., pp. 5.

Dominy, S.C., Platten, M., 2011. BCGold Corporation: Engineer Gold Project, BC, Canada – Project No. L502 – Mineral Resource Estimate – April 2011. NI 43-101 technical report prepared for BCGold Corp by Snowden Mining Industry Consultants, pp. 96.

Dong, G., Morrison, G.W., 1995. Adularia in epithermal veins, Queensland: morphology, structural state and origin. Mineral. Deposita 30, 11–19.

Dong, G., Morrison, G., Jaireth, S., 1995. Quartz Textures in Epithermal Veins, Queensland – Classification, Origin, and Implication. Economic Geology 90, 1841-1856.

Drever, H.I.J., Butler, P., Gibb, F.G.F., 1972. Some textures in Apollo 12 lunar igneous rocks and in terrestrial analogs. Proceedings of the Third Lunar Science Conference, Supplement 3, Geochimica et Cosmochimica Acta 1, 171-184.

Drummond, S.E., Ohmoto, H., 1985. Chemical evolution and mineral deposition in boiling hydrothermal systems. Economic Geology 80, 126–147.

Fleet, M.E., Mumin, A.H., 1997. Gold-bearing arsenian pyrite and marcasite and arsenopyrite from Carlin Trend gold deposits and laboratory synthesis. American Mineralogist 82, 182–193.

Fournier, R.O., 1985. Carbonate Transport and Deposition in the Epithermal Environment. In Berger, B.R., Bethke, P.M. (eds.): Geology and geochemistry of epithermal systems. Reviews in Economic Geology 2, 63-72.

GEOROC, 2015. GEOROC – Geochemistry of Rocks of the Oceans and Continents. Website: http://georoc.mpch-mainz.gwdg.de/georoc/

Guggenheim, S., Bain, D.C., Bergaya, F., Brigatti, M.F., Drits, V.A., Eberl, D.D., Formoso, M.L.L., Galán, E., Merriman, R.J., Peacor, D.R., Stanjek, H., Watanabe, T., 2002. Report of the Association Internationale pour l'Etude des Argiles (AIPEA) Nomenclature Committee for 2001: Order, disorder and crystallinity in phyllosilicates and the use of the "Crystallinity Index." Clay Minerals 37, 389–393.

Han, X.J., Wei, B., n.d. Microstructural characteristics of Ni-Sb eutectic alloys under substantial undercooling and containerless solidification conditions. Metall and Mat Trans A 33, 1221–1228.

Hedenquist. J.W., Arribas R., A., Gonzaley-Urien, E., 2000. Exploration for Epithermal Gold Deposits. SEG Reviews 13, 245-277.

Heinrich, C.A., 2007. Fluid-Fluid Interactions in Magmatic-Hydrothermal Ore Formation. Reviews in Mineralogy and Geochemistry 65, 363–387.

Henley, R.W., 1993. Epithermal gold deposits in volcanic terranes. In Foster, R.P. (ed.): Gold Metallogeny and Exploration, 133-164.

Herdianita, N.R., Browne, P.R.L., Rodgers, K.A., Campbell, K.A., 2000. Mineralogical and textural changes accompanying ageing of silica sinter. Mineral. Deposita 35, 48–62.

Herrington, R.J. and Wilkinson, J.J., 1993. Colloidal gold and silica in mesothermal vein systems. Geology 21, 539–542.

Irvine, T.N. and Baragar, W.R.A., 1971. A Guide to Chemical Classification of the Common Volcanic Rock. Canadian Journal of Earth Sciences, 8, 523-548.

Jensen, E., 2008. Site Visit to Engineer Mine, Tagish Lake, British Columbia; Summary and Recommendations. Internal company report for BCGold Corp., pp. 13.

Jensen, E.P., Barton, M.D., 2000. Gold deposits related to alkaline magmatism. Reviews in Economic Geology 13, 279–314.

Keith, H.D., Padden, Jr, F.J., 2004. Spherulitic Crystallization from the Melt. I. Fractionation and Impurity Segregation and Their Influence on Crystalline Morphology. Journal of Applied Physics 35, 1270–1285.

Le Bas, M.J., Le Maitre, R.W., Streckeisen, A., Zanettin. B., 1986. A chemical classification of volcanic rocks based on the total alkali-silica diagram. Journal of Petrology 27, 745- 750.

Leitch, C.H.B., 2012. Petrographic Report on 5 Samples from Engineer Project. Internal company report for BCGold Corp., pp. 10.

Lofgren, G., 1974. An Experimental Study of Plagioclase Crystal Morphology: Isothermal Crystallization. American Journal of Science 274, 243-273.

Love, D.A., 1997. The Mount Skukum epithermal gold deposit and its geological setting, Yukon Territory, Canada. Ph.D. thesis, Queen's University, Kingston, Ontario, Canada, pp. 545.

Lovering, T.G., 1972. Jasperoid in the United States; its characteristics, origin, and economic significance (No. PP - 710). United States Geological Survey.

Mauthner, H.F., Groat, L.A., Raudsepp, M., 1996. The Engineer Mine – Tagish Lake, British Columbia. The Mineralogical Record 27, July-August, 1996, 263-273.

McDonald, B.W.R., 1987. Geology and Genesis of the Mount Skukum Tertiary Epithermal Godl-Silver Vein Deposit, Southwestern Yukon Territory (NTS 105D SW). Ph.D. thesis, University of British Columbia, Canada, pp. 197.

Meunier, A., Velde, B., 2004. Illite. Springer-Verlag Berlin Heidelberg GmbH, pp. 286.

Mihalynuk, M. G., Mountjoy, K.J., Smith, M.T., Currie, L.D., Gabites, J.E., Tipper, H.W., Orchard, M.J., Poulton, T.P., Cordey, F., 1999a. Geology and mineral resources of the Tagish Lake area (NTS 104M/8, 9, 10E, 15 and 104N/12W), northwestern British Columbia. British Columbia Ministry of Energy and Mines, Energy and Minerals Divison, Geological Survey Branch, Bulletin 105, pp. 217.

Mihalynuk, M.G., Hart, C.J.R., Friedman, R.M., Gabites, J.E., and Mortensen, J.K., 1999b. Sloko Group, northwest British Columbia, southwest Yukon; unpublished manuscript.

Moncada, D., Mutchler, S., Nieto, A., Reynolds, T.J., Rimstidt, J.D., Bodnar, R.J., 2012. Mineral textures and fluid inclusion petrography of the epithermal Ag–Au deposits at Guanajuato, Mexico: Application to exploration. Journal of Geochemical Exploration 114, 20–35.

Morris, G.A., Creaser, R.A., 2003. Crustal recycling during subduction at the Eocene Cordilleran margin of North America: a petrogenetic study from the southwestern Yukon. Can. J. Earth Sci. 40, 1805–1821.

O'Neil, J.R., Clayton, R.N., Mayeda, T.K., 2003. Oxygen Isotope Fractionation in Divalent Metal Carbonates. The Journal of Chemical Physics 51, 5547–5558.

Oaki, Y., Imai, H., 2003. Experimental Demonstration for the Morphological Evolution of Crystals Grown in Gel Media. Crystal Growth & Design 3, 711–716.

Oehler, J.H., 1976. Hydrothermal crystallization of silica gel. Geological Society of America Bulletin 87, 1143–1152.

Pan, Y., Fleet, M.E., 1992. Mineral chemistry and geochemistry of vanadian silicates in the Hemlo gold deposit, Ontario, Canada. Contr. Mineral. and Petrol. 109, 511–525.

Passchier, C.W. and Trouw, R.A.J., 2005. Microtectonics, 2nd Edition. Springer, Berlin ; New York, pp. 366.

Pearce, J.A., 1996. A User's Guide to Basalt Discrimination Diagrams, in Wynman, D.A., ed., Trace Element Geochemistry of Volcanic Rocks: Applications for Massive Sulphide Exploration: Geological Association of Canada, Short Course Notes, v.12, 79-113.

Petruk, W., Cabri, L.J., Harris, D.C., Stewart, J.M., Clark, L.A., 1970. Allargentum, Redefined. Can Mineral 10, 163–172.

Putnis, A., 2009. Mineral Replacement Reactions. Reviews in Mineralogy and Geochemistry 70, 87–124.

Qiu, J.-T., Song, W.-J., Jiang, C.-X., Wu, H., Dong, R.M., 2013. CGDK: An extensible CorelDRAW VBA program for geological drafting. Computers & Geosciences 51, 34–48.

Ramdohr, P., 1980. Ingerson, D.E. (ed.). The Ore Minerals and their Intergrowths - 2nd Edition – Volume I, Pergamon Press, pp. 1202.

Reich, M., Kesler, S.E., Utsunomiya, S., Palenik, C.S., Chryssoulis, S.L., Ewing, R.C., 2005. Solubility of gold in arsenian pyrite. Geochimica et Cosmochimica Acta 69, 2781–2796.

Rennie, D.W., Collins, S.E., Altman, K.A., 2012. Technical Report on the Porgera Joint Venture, Enga Province, Papua New Guinea. Ni 43-101 report prepared for Barrick Gold Corporation, dated March 16, 2012, pp. 210.

Richards, J.P., 1995. Alkalic-type epithermal gold deposits—a review: Mineralogical Association of Canada Short Course 23, 367–400.

Rieder, M., Cavazzini, G., D'yakonov, Y.S., Frank-Kamenetskii, V.A., Gottardi, G., Guggenheim, S., Koval', P.V., Mueller, G., Neiva, A.M.R., Radoslovich, E.W., Robert, J.-L., Sassi, F.P., Takeda, H., Weiss, Z., Wones, D.R., 1998. Nomenclature of the micas. Can Mineral 36, 905–912.

Sander, M.V., Black, J.E., 1988. Crystallization and Recrystallization of Growth-zoned Vein Quartz Crystals From Epithermal Systems – Implications for Fluid Inclusion Studies. Economic Geology 83, 1052-1060.

Schroeter, T.G., 1986. Bennet Project (104M). British Columbia Ministry of Energy, Mines and Petroleum Resources, Geological Fieldwork, 1985, Paper, 1986-1, 185-189.

Seward, T.M., 1993. The hydrothermal geochemistry of gold. In Foster, R.P. (ed.): Gold Metallogeny and Exploration, 37-62.

Sheppard, S.M.F., Gilg, H.A., 1996. Stable Isotopes Geochemistry of Clay Minerals. Clay Minerals 31, 1-24.

Sibson, R.H., 1987. Earthquake rupturing as a mineralizing agent in hydrothermal systems. Geology 15, 701-704.

Sillitoe, R.H., Hedenquist, J.W., 2003. Linkages between Volcanotectonic Settings, Ore-Fluid Compositions, and Epithermal Precious Metal Deposits. Society of Economic Geologists, Special Publication 10, 315-343.

Simmons, S.F., Christenson, B.W., 1994. Origins of calcite in a boiling geothermal system. Am J Sci 294, 361–400.

Simmons, S.F., Browne, P.R.L., 2000. Hydrothermal Minerals and Precious Metals in the Broadlands-Ohaaki Geothermal System: Implications for Understanding Low-Sulfidation Epithermal Environments. Economic Geology 95, 971–999.

Smit, H., 1988. Diamond Drilling Report on the Engineer Property – Atlin Mining Division – British Columbia. Internal report prepared for Erickson Gold Mining Corp., pp. 283.

Staude, S., Wagner, T., Markl, G., 2007. Mineralogy, Mineral Compositions and Fluid Evolution at the Wenzel Hydrothermal Deposit, Southern Germany: Implications for the Formation of Kongsberg-Type Silver Deposits. Can Mineral 45, 1147–1176.

Suzuoki, T., Epstein, S., 1976. Hydrogen isotope fractionation between OH-bearing minerals and water. Geochimica et Cosmochimica Acta 40, 1229–1240.

Tiller, W.A., 1956. Alloy Dendritic Growth. Can. J. Phys. 34, 729–730.

Tosdal, R.M., Dilles, J.H., Cooke, D.R., 2009. From Source to Sinks in Auriferous Magmatic-Hydrothermal Porphyry and Epithermal Deposits. ELEMENTS 5, 289–295.

Williams-Jones, A.E., Bowell, R.J., Migdisov, A.A., 2009. Gold in Solution. ELEMENTS 5, 281–287.

Winchester, J.A., Floyd, P.A., 1977. Geochemical discrimination of different magma series and their differentiation products using immobile elements. Chemical Geology 20, 325–343.